



**Michigan
Technological
University**

Michigan Technological University
Digital Commons @ Michigan Tech

Michigan Tech Publications, Part 2

1-4-2024

Designing a Convection-Cloud Chamber for Collision-Coalescence Using Large-Eddy Simulation With Bin Microphysics

Aaron Wang
Pacific Northwest National Laboratory

Mikhail Ovchinnikov
Pacific Northwest National Laboratory

Fan Yang
Brookhaven National Laboratory

Silvio Schmalfluss
Leibniz Institute for Tropospheric Research

Raymond A. Shaw
Michigan Technological University, rashaw@mtu.edu

Follow this and additional works at: <https://digitalcommons.mtu.edu/michigantech-p2>



Part of the [Physics Commons](#)

Recommended Citation

Wang, A., Ovchinnikov, M., Yang, F., Schmalfluss, S., & Shaw, R. (2024). Designing a Convection-Cloud Chamber for Collision-Coalescence Using Large-Eddy Simulation With Bin Microphysics. *Journal of Advances in Modeling Earth Systems*, 16(1). <http://doi.org/10.1029/2023MS003734>
Retrieved from: <https://digitalcommons.mtu.edu/michigantech-p2/552>

Follow this and additional works at: <https://digitalcommons.mtu.edu/michigantech-p2>



Part of the [Physics Commons](#)



RESEARCH ARTICLE

10.1029/2023MS003734

Designing a Convection-Cloud Chamber for Collision-Coalescence Using Large-Eddy Simulation With Bin Microphysics

Aaron Wang¹ , **Mikhail Ovchinnikov¹** , **Fan Yang²** , **Silvio Schmalfuss³** , and **Raymond A. Shaw⁴**
¹Pacific Northwest National Laboratory, Richland, WA, USA, ²Brookhaven National Laboratory, Upton, NY, USA,³Leibniz Institute for Tropospheric Research, Leipzig, Germany, ⁴Michigan Technological University, Houghton, MI, USA**Key Points:**

- Collision-coalescence effects on a steady-state droplet size distribution are stronger in a taller chamber
- Wet side walls are essential for maintaining cloud liquid water in a chamber with a low width-to-height aspect ratio
- Rougher surfaces increase surface heat and moisture fluxes, leading to larger liquid water content that promotes collision-coalescence

Supporting Information:

Supporting Information may be found in the online version of this article.

Correspondence to:

A. Wang and M. Ovchinnikov,
aaron.wang@pnnl.gov;
Mikhail.Ovchinnikov@pnnl.gov

Citation:

Wang, A., Ovchinnikov, M., Yang, F., Schmalfuss, S., & Shaw, R. A. (2024). Designing a convection-cloud chamber for collision-coalescence using large-eddy simulation with bin microphysics. *Journal of Advances in Modeling Earth Systems*, 16, e2023MS003734. <https://doi.org/10.1029/2023MS003734>

Received 4 APR 2023

Accepted 4 JAN 2024

Author Contributions:

Conceptualization: Aaron Wang, Mikhail Ovchinnikov, Fan Yang, Silvio Schmalfuss, Raymond A. Shaw

Data curation: Aaron Wang

Formal analysis: Aaron Wang, Mikhail Ovchinnikov, Fan Yang, Silvio Schmalfuss, Raymond A. Shaw

Funding acquisition:

Mikhail Ovchinnikov

Abstract Collisional growth of cloud droplets is an essential yet uncertain process for drizzle and precipitation formation. To improve the quantitative understanding of this key component of cloud-aerosol-turbulence interactions, observational studies of collision-coalescence in a controlled laboratory environment are needed. In an existing convection-cloud chamber (the Pi Chamber), collisional growth is limited by low liquid water content and short droplet residence times. In this work, we use numerical simulations to explore various configurations of a convection-cloud chamber that may intensify collision-coalescence. We employ a large-eddy simulation (LES) model with a size-resolved (bin) cloud microphysics scheme to explore how cloud properties and the intensity of collision-coalescence are affected by the chamber size and aspect ratio, surface roughness, side-wall wetness, side-wall temperature arrangement, and aerosol injection rate. Simulations without condensation and evaporation within the domain are first performed to explore the turbulence dynamics and wall fluxes. The LES wall fluxes are used to modify the Scalar Flux-budget Model, which is then applied to demonstrate the need for non-uniform side-wall temperature (two side walls as warm as the bottom and the two others as cold as the top) to maintain high supersaturation in a tall chamber. The results of LES with full cloud microphysics reveal that collision-coalescence is greatly enhanced by employing a taller chamber with saturated side walls, non-uniform side-wall temperature, and rough surfaces. For the conditions explored, although lowering the aerosol injection rate broadens the droplet size distribution, favoring collision-coalescence, the reduced droplet number concentration decreases the frequency of collisions.

Plain Language Summary A convection-cloud chamber is useful in understanding how turbulence affects the interaction between aerosols and cloud droplets. The current convection-cloud chamber (the Pi Chamber) is likely too small to explore how turbulence affects the collision-coalescence among cloud droplets. To see whether collisional growth may be observable in a larger cloud chamber, we use numerical simulations to model the cloud droplet size distributions under several different configurations of the cloud chamber. The results suggest that the likelihood of detectable collisional growth increases significantly in a tall chamber with two warm and two cold saturated side walls and rough wall surfaces.

1. Introduction

A convection-cloud chamber, such as the Pi Chamber at the Michigan Technological University (Chandrakar et al., 2016; Chang et al., 2016), is a valuable tool for exploring cloud-aerosol-turbulence interactions that play an important yet not well quantified role in the cloud-aerosol radiative forcing in climate (e.g., Szopa et al., 2021) and severe weather systems (e.g., the evaporative cooling for the cold-pool outflow which enhances the low-level mesocyclones of a convective storm, Brooks, Doswell, & Cooper, 1994; Brooks, Doswell, & Wilhelmson, 1994; Mallinson & Lasher-Trapp, 2019; Murdzek et al., 2022). For example, the Pi Chamber has been used to investigate the broadening of a droplet size distribution (DSD) induced by supersaturation fluctuations in a turbulent cloud (Chandrakar et al., 2016, 2018), which is consistent with the observed DSDs in real clouds being broader than predicted by a simple diffusional growth theory using constant supersaturation (Blyth, 1993; Schmeissner et al., 2015). Although the Pi Chamber has been successful in reproducing a number of cloud-aerosol-turbulence interactions related to droplet activation, condensational growth, and evaporation, its application to studying collision-coalescence is limited. Both observed (Chandrakar et al., 2016) and modeled (Thomas et al., 2023) DSDs in the Pi chamber show little evidence of collision-coalescence effects, likely because

© 2024 Battelle Memorial Institute and Leibniz Institute for Tropospheric Research e.V. and The Authors. *Journal of Advances in Modeling Earth Systems* published by Wiley Periodicals LLC on behalf of American Geophysical Union. This is an open access article under the terms of the [Creative Commons Attribution-NonCommercial-NoDerivs License](https://creativecommons.org/licenses/by/4.0/), which permits use and distribution in any medium, provided the original work is properly cited, the use is non-commercial and no modifications or adaptations are made.

Investigation: Aaron Wang
Methodology: Aaron Wang, Mikhail Ovchinnikov
Project administration: Mikhail Ovchinnikov, Raymond A. Shaw
Resources: Mikhail Ovchinnikov
Software: Aaron Wang, Mikhail Ovchinnikov, Fan Yang
Supervision: Mikhail Ovchinnikov
Validation: Aaron Wang
Visualization: Aaron Wang
Writing – original draft: Aaron Wang, Mikhail Ovchinnikov
Writing – review & editing: Aaron Wang, Mikhail Ovchinnikov, Fan Yang, Silvio Schmalfuss, Raymond A. Shaw

of limited steady-state liquid water content (LWC) and short droplet residence time within the chamber's domain of $2 \times 2 \times 1 \text{ m}^3$.

Collision-coalescence is an important mechanism contributing to the broadening of a DSD and subsequent initiation and further development of precipitation (e.g., Hsieh et al., 2009; Magaritz-Ronen et al., 2016). Among the rain production processes, the initial formation of drizzle-size droplets is perhaps the most uncertain. Collisions among cloud droplets require a relative velocity between them, but the droplets' gravitational terminal velocities are small. Turbulence can increase the relative velocity of droplets, and studies have shown that the collision efficiency in a turbulent flow can be several times higher than in a calm atmosphere (e.g., Pinsky et al., 1999, 2000). In addition to turbulence, collisional growth can also be influenced by electrical charge (Lu & Shaw, 2015). Upon a collision event, two droplets may coalesce into one larger droplet, bounce apart, or break into smaller droplets owing to their original momentum (e.g., Stensrud, 2007).

In numerical simulations, the collision-coalescence process is mainly controlled by the collision kernel (efficiency), which is derived from the assumption that two droplets are interacting in a Stokes flow (e.g., Klett & Davis, 1973; Lin & Lee, 1975; Schlamp et al., 1976), and it can be modified by accounting for the influence of other factors, such as turbulence. However, even the calculations in low-Reynolds-number flow have demonstrated inconsistency to a certain degree (see Figure 1 in Schlamp et al., 1976), not to mention the added complexity imposed by turbulence. As a result, the collision-coalescence model in cloud simulations remains a significant source of uncertainty. Fan et al. (2017) conducted an intercomparison of cloud-resolving models, showing that variations in the rain rate can be largely attributed to different parameterizations of the collision-coalescence process. Moreover, using the same dynamical core, Hill et al. (2023) carried out a sensitivity test on various microphysics schemes, revealing that collision-coalescence is a major factor contributing to discrepancies in the simulated liquid water path, DSDs, and precipitation rates. In short, given the numerous uncertainties in precipitation predictions due to the collision-coalescence process, there is a critical need for a laboratory facility capable of observing and quantifying the droplet collision-coalescence process in turbulent flow.

The purpose of this work is to explore configuration options that would make a convection-cloud chamber suitable for studying collision-coalescence. The study is based on a large-eddy simulation (LES) model that was developed for the Pi-Chamber conditions (Thomas et al., 2019; Yang et al., 2022). Our primary focus is on identifying modifications to the chamber setup that can increase the steady-state LWC. The dominant effect of LWC on collision-coalescence is supported by theoretical considerations. It can be shown, for example, that under the assumption of an analytical collection kernel (Long, 1974) for small droplets (radius less than $50 \mu\text{m}$), the collisional rate of cloud droplets scales with the LWC squared (e.g., Kostinski & Shaw, 2005; Wood, 2006). The strong effect of cloud LWC on drizzle and rain through collision-coalescence is also reflected in theoretical and empirical parameterizations of the so-called autoconversion process. In formulations commonly used in cloud and global models, the autoconversion rate is a function of the LWC to the power of 2 to over 4 (e.g., Chiu et al., 2021; M. Khairoutdinov & Kogan, 2000; Kogan, 2013). Several factors controlling LWC in a convection-cloud chamber have previously been identified. These factors can be grouped into three categories: chamber geometry, boundary conditions for temperature and moisture, and aerosol injection rate, which is a primary control for the droplet number concentration.

Theoretical considerations and numerical modeling suggest that increasing the height of the chamber leads to longer droplet residence times, thereby enhancing the probability of collisions (Chang et al., 2016; Shaw et al., 2020; Thomas et al., 2023). Thomas et al. (2023) used LES to show that scaling the Pi chamber up with a fixed DSD and a fixed aspect ratio of the chamber (defined as the ratio of width to height) promotes collision-coalescence. However, scaling up the domain with the same aspect ratio rapidly increases the chamber volume, which would complicate the construction and operation of such a facility. For example, the 8-m high chamber in Thomas et al. (2023) has a cross area of $16 \times 16 \text{ m}^2$ and would require large supplies of energy, water, and aerosol to maintain a cloud in $2,048\text{-m}^3$ volume. Therefore, a chamber with a lower aspect ratio could be a more practical alternative, as we examine in this study.

Reducing the aspect ratio of a cloud chamber increases the influence of the side walls. Side walls with a uniform temperature within a range between top and bottom temperatures limit the supersaturation achievable in a chamber without a cloud (see Figures 1 and 2 in Thomas et al., 2019) and the LWC under cloudy conditions. The effect is especially pronounced when the side walls are not completely wet. An alternate approach is to apply a

temperature difference across the water-saturated side walls as well as between the top and bottom of the convection chamber, thereby allowing the side walls to augment rather than deplete the supersaturation field. Thermal convection driven by side walls is typically referred to as vertical convection or tilted Rayleigh-Bénard convection, and has been studied in the literature (Chand et al., 2022; Shishkina, 2016; Q. Wang et al., 2021). We will build on that work by exploring how various specifications of side wall temperature and moisture can enhance the supersaturation, the LWC, and as a consequence the droplet collision rate. Additionally, differential heating of the side walls may enhance the large-scale circulation (e.g., Ng et al., 2015) and alter the conditions in the chamber. The possible parameter space is enormous, and in this work we include simulations with saturated side walls with an applied temperature difference equal to that between the top and bottom walls.

The steady-state LWC may also depend on the moisture fluxes from the walls. Moisture fluxes carried by near-surface turbulence can be increased over rougher surfaces. Specifically, a rougher surface increases fluxes of momentum, heat, and moisture (Toppaladoddi et al., 2015; Tummers & Steunebrink, 2019; Zhu et al., 2019), leading to an overall higher turbulence kinetic energy (TKE), more intense mixing, and potentially to a larger LWC. Thus, this work also tests different roughness lengths for the walls.

Apart from being influenced by the domain shape and walls' properties, cloud microphysics and, therefore, collision-coalescence rate depend strongly on the concentration of cloud condensation nuclei (CCN) and the resulting droplet concentration. A lower concentration of CCN results in a broader DSD, which favors collision-coalescence because of increased differences in the droplets' terminal velocities. Yet, the reduced droplet number concentration simultaneously reduces the frequency of droplet collisions, thus increasing the difficulty of observing their collisional growth. In a cloud chamber, the concentration of available CCN is controlled primarily by the aerosol injection rate, which, under steady-state conditions, is balanced by the droplet removal rate by sedimentation. Note that in Thomas et al. (2023), the aerosol injection rate was modified to keep the droplet number concentration nearly the same in chambers of different sizes to maintain consistency of the microphysics regime (defined by the ratio of turbulent-correlation time to phase-relaxation time, Chandrakar et al., 2016). In this work, for the purpose of illustrating the dependencies of sensitivities to one more setup parameter, we apply two aerosol injection rates to various chamber configurations.

While beyond the scope of this work, it is worth noting whether the numerical methods could lead to the broadening of DSDs. Although Morrison et al. (2018) have shown the artificially enhanced broadening of DSDs associated with vertical diffusion in a Eulerian dynamical model, Yang et al. (2022) find that the impact of numerical broadening of the DSDs in the cloud-chamber LES is very small due to the relatively fine grid spacing, short time step, and weak vertical velocity compared to convection in an atmospheric boundary layer. Additionally, Yang et al. (2023) shows that the cloud-chamber LES results from an Eulerian bin microphysics scheme agree well with those from a Lagrangian microphysics scheme, and the latter does not experience numerical diffusion. To narrow the scope of this study, we will focus on the sensitivity of the results to the chamber configurations rather than numerical methods.

In this study, exploration of the broad parameter space is conducted mainly using LES, which resolves energy-carrying eddies and fluctuations and predicts the evolution of cloud droplets of different sizes using a bin microphysics scheme. Recently, Thomas et al. (2019) scaled down an atmospheric LES model (System for Atmospheric Modeling, SAM, M. F. Khairoutdinov & Randall, 2003) combined with a bin microphysics scheme (Khain et al., 2004) to simulate the Pi Chamber and explore its turbulence and cloud properties. Here, we employ the same model with modified domain configurations, grid spacing, and treatment of boundary conditions.

In addition to LES, we use results from direct numerical simulations (DNS), both new and those conducted previously (Chandrakar et al., 2022), to determine the wall-model parameters for surface flux calculation in LES. A DNS model is not used to perform the sensitivity simulations in this work due to its demanding computational cost and the lack of efficient ways to handle microphysics and surface roughness. Lastly, we include the application of a Scalar Flux-budget Model (SFM), which has been used in cloud-chamber related works (Thomas et al., 2019). As an analytical model, the SFM is capable of predicting domain-mean fields for input parameters varying continuously over a specified range, which can only be sparsely sampled with time-consuming LES. In this study, we use LES to improve the accuracy of the SFM and apply it to obtain a continuous relationship between the chamber's aspect ratio and the mean supersaturation in the chamber. These SFM results illustrate why non-uniform side-wall temperatures are desired.

The rest of this article is arranged as follows. Section 2 describes the LES model and configurations of all simulations. Section 3 presents the LES results of moist, cloud-free simulations and their application to improve the SFM. Section 4 presents analysis of the cloudy LES results. Section 5 presents the conclusion. Appendix A provides the temporal evolution of some flow properties to show the quasi-steady states. Appendix B illustrates how we determine the roughness length of the wall model. Appendix C demonstrates how we determine the side-wall wetness. Finally, Appendix D provides some dimensionless parameters for comparison with the literature.

2. LES Configurations

The LESs are performed using SAM (M. F. Khairoutdinov & Randall, 2003). The momentum equations are solved on an Arakawa C-grid with an anelastic approximation, a 1.5-order TKE subgrid-scale (SGS) model, and a second-order-central advection scheme. The scalars (temperature, microphysical fields, and SGS TKE) are advected using a multidimensional positive definite advection transport algorithm (Smolarkiewicz & Grabowski, 1990), which is chosen as it has been widely used in the study of cloud-chamber simulations (Thomas et al., 2019; Yang et al., 2022, 2023). Although the sensitivity to the advection scheme is beyond the scope of this study, it is worth noting that a less diffusive advection scheme has been found to produce a higher number concentration and LWC (Yang et al., 2022). The eddy diffusivity for scalars in the interior of the domain is derived by assuming a turbulent Prandtl number of 1 (i.e., Reynolds analogy, Kays et al., 1980).

For the boundary conditions of the momentum and temperature equations (i.e., the momentum and heat fluxes of the walls), the Monin-Obukhov similarity theory (MOST, Monin & Obukhov, 1954) is applied to local grid points with necessary modifications. Specifically, the input Richardson number is set to 0 for the side walls because the influence of buoyancy is parallel instead of normal to the side walls (i.e., the influence of buoyancy is already on the accelerated wall-parallel velocity which is used to model the wall fluxes). This is equivalent to applying the law of the wall for surface shear stress on the side walls (Prandtl, 1933). In addition, the original MOST parameterization implementation in SAM sets a minimum of $\sqrt{0.5} (\approx 0.71) \text{ m s}^{-1}$ for the near-surface wind speed. While this limit may be appropriate for typical atmospheric boundary layers, it is higher than the velocity scale in the Pi Chamber ($\sim 0.1 \text{ m s}^{-1}$) and leads to an overestimation of the surface fluxes. To address this issue, we lowered the minimum input near-surface wind speed to 0.01 m s^{-1} , which is required for the grid spacing of $\sim 1 \text{ cm}$ and $z u_* / \nu > 30$ to ensure the validity of the law of the wall (the neutral situation of MOST), as described by Pope (2000). Here z refers to the distance from the wall, u_* is the friction velocity, and ν is the kinematic viscosity.

The roughness length and side-wall wetness are different from those applied in Thomas et al. (2019). The side-wall wetness is defined as the saturation ratio of air at the side wall temperature. The roughness length is set to 0.75 mm for momentum (z_0), for temperature to $z_t = 0.619 z_0$, and for moisture to $z_q = 0.756 z_0$. This value for z_0 is found by performing LES following the configuration of DNS by Chandrakar et al. (2022) and matching the Nusselt and Sherwood numbers of our LES to their DNS (see Appendix B for details). The relationships among the roughness lengths of momentum, temperature, and moisture are found by performing a set of additional DNS, which are similar to those found in a channel flow with rough walls (Brutsaert, 1982; Garratt, 1994). The top and bottom walls are saturated with respect to liquid water in all presented simulations. The side walls, if not saturated, have a wetness of 0.39 in simulations using 6.25 cm grid spacing and 0.50 for the simulations with 3.125 cm grid spacing. These values are chosen to match the mean bulk supersaturation of 2.5%, as observed in the Pi Chamber when no droplets exist (see Appendix C for details).

The cloud microphysics is handled using the same bin model as in Thomas et al. (2019), which is developed by the Hebrew University of Jerusalem group and described in detail in Khain et al. (2004). An evolution of aerosol and droplet spectra is represented by predicting number concentrations in each of the 33 mass-doubling size bins. Particles are transferred from the aerosol to the first bin of droplet category during droplet activation when the ambient supersaturation exceeds the critical values for a given aerosol particle size. Following activation, the DSD evolves under microphysical processes of diffusional growth and evaporation, collision-coalescence, and breakup, as well as sedimentation, advection, and mixing. The collision kernel at three different pressure levels (1,000, 750, and 500 mb) is calculated by Pinsky et al. (2001), the turbulence factors that increase the collision kernels are derived by Khain et al. (2004) (see its Table 1), and the collisional breakup is parameterized based on Low and List (1982) and Beard and Ochs (1995) (see more details in Khain et al., 2004; Seifert et al., 2005).

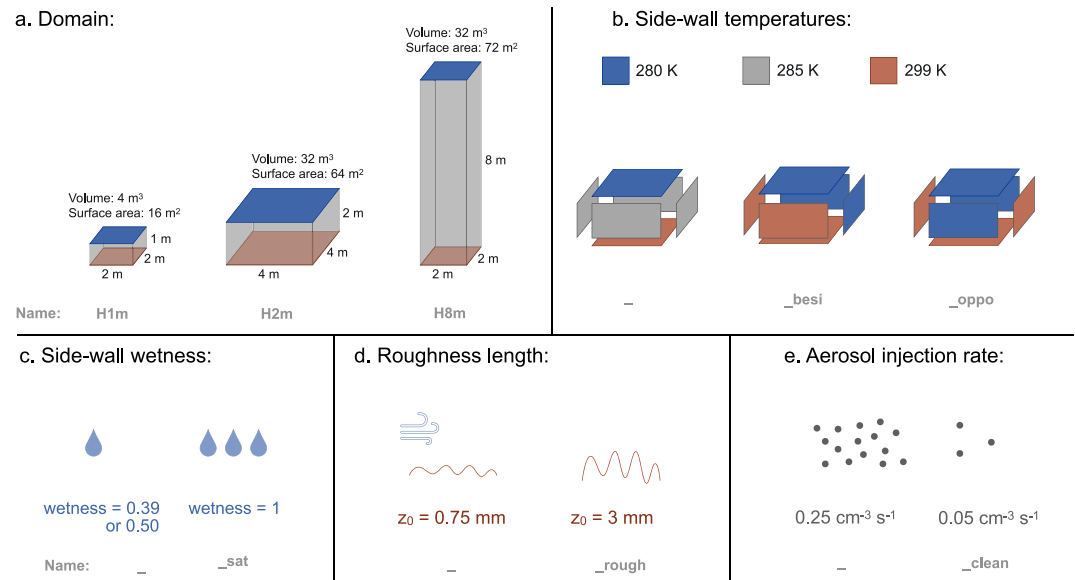


Figure 1. Illustration of the sensitivity tests and how they are indicated by the case names.

The domain to mimic the Pi Chamber is a 2 m × 2 m × 1 m box. The air is initially still with linear profiles of temperature and specific humidity between the top and bottom walls. To test the sensitivity to spatial resolution, two simulations of the Pi Chamber are first performed: one with a 3.125-cm grid spacing (as used in Thomas et al., 2019), and another with a grid spacing of 6.25 cm. Each case is simulated for 1 hr with a dynamic time step satisfying the Courant-Friedrichs-Lewy criterion. Given small quantitative differences in the chamber-mean properties and significant differences in the required computing resources between simulations with the two grid spacings, the 6.25 cm grid spacing is used in this study for the sensitivity tests to explore various domain shapes, surface roughnesses, non-uniform arrangements of side-wall temperatures, side-wall wetnesses, and injection rates.

The geometries of the tested domains are 2 m × 2 m × 1 m, 4 m × 4 m × 2 m, and 2 m × 2 m × 8 m. In the simulation names, these are indicated by their heights as H1m, H2m, and H8m, respectively (Figure 1a). Note that H2m and H8m have the same volume (32 m³), but H8m has a larger wall surface area.

The temperatures of the top and bottom surfaces for all simulations are fixed at 280 and 299 K, respectively (Chang et al., 2016; Thomas et al., 2019). In the baseline simulations, the side-wall temperature is uniformly 285 K. Two non-uniform side-wall temperature arrangements are also tested: (a) the left and front side walls are 299 K, and the right and back walls are 280 K; (b) the left and right walls are 299 K, and the front and back walls are 280 K (Figure 1b). These arrangements are indicated in case names by “besi” and “oppo,” respectively, reflecting the side walls with the same temperature being beside or opposite each other.

Simulations with the saturated side walls are indicated by “sat” in the case name (Figure 1c). Also, in addition to the baseline roughness length, z₀ = 0.75 mm, a rougher surface with z₀ = 3 mm is tested (indicated as “rough” in case names) to explore the influence of increased shear production of turbulence (both resolved and unresolved) and fluxes on the wall (Figure 1d).

Lastly, to examine the influence of aerosol concentration, two aerosol injection rates are compared for the cases that produce significantly more collision-coalescence in the above-mentioned sensitivity tests. The baseline injection rate is 0.25 cm⁻³ s⁻¹, and a cleaner experiment has an injection rate of 0.05 cm⁻³ s⁻¹ (indicated as “clean” in the case name). A wall-loss timescale ($t_{\text{wall_loss}}$) is applied to constrain the aerosol concentration as

$$\frac{\partial N_A}{\partial t} = N_A \left(1 - \frac{\Delta t}{t_{\text{wall_loss}}} \right), \quad (1)$$

Table 1
Configurations of the Moist (No-Cloud) Simulations

Case	Δx (cm)	Height (m)	Width (m)	z_0 (mm)
H1m ₀	3.125	1	2	0.75
H1m	6.25	1	2	0.75
H1m_rough	6.25	1	2	3
H2m	6.25	2	4	0.75
H2m_rough	6.25	2	4	3
H8m	6.25	8	2	0.75
H8m_rough	6.25	8	2	3

Note. The side walls are at 285 K and saturated with respect to liquid water.

where N_A is the number concentration of aerosol and Δt is the time step of the simulation. The timescale $t_{\text{wall_loss}}$ is set to 10 min, as in Thomas et al. (2019).

The different domains and surface roughnesses are at first tested without microphysics (i.e., moist simulations) to evaluate wall fluxes and attainable supersaturation and compare them with the SFM (Thomas et al., 2019). The tested configurations of the moist simulations are listed in Table 1. Then, the simulations with the full microphysics (i.e., cloudy simulations) are performed to test the sensitivity to various domains, side-wall temperature arrangements, side-wall wetnesses, surface roughnesses, and aerosol injection rates. The details of the cloudy simulations are listed in Table 2. Lastly, the default case (H1m) and some cases with significantly broader DSDs are performed again with the collision process turned off to reveal the collisional broadening in the DSDs.

3. Results of Moist Simulations

Moist simulations (considering water vapor but not the liquid phase processes) are first used to explore turbulence properties, wall fluxes, and the resulting supersaturation. Note that in the actual Pi chamber, such conditions are realized when aerosol is not injected into the chamber and, consequently, no droplets are formed. Specifically, this section shows the modeled TKE, heat and moisture fluxes, and resulting supersaturation during the quasi-steady state for various chamber configurations (note that the differential side-wall temperature forcing is not considered in the moist simulations). The background supersaturation acts as the driving force for cloud formation (Chandrakar et al., 2016, 2018), so the trend of supersaturation provides us with an indication of whether cloud formation will increase or decrease. In addition, the results from the moist simulations provide simplified outcomes

Table 2
Configurations of the Cloudy Simulations

Case	Δx (cm)	Height (m)	Width (m)	Side-wall temperature	Side-wall wetness	z_0 (mm)	Aerosol injection rate (s^{-1})
H1m ₀	3.125	1	2	Uniform	0.50	0.75	0.25
H1m	6.25	1	2	Uniform	0.39	0.75	0.25
H2m	6.25	2	4	Uniform	0.39	0.75	0.25
H2m_sat	6.25	2	4	Uniform	1	0.75	0.25
H2m_sat_rough	6.25	2	4	Uniform	1	3	0.25
H2m_sat_rough_clean	6.25	2	4	Uniform	1	3	0.05
H2m_besi	6.25	2	4	Beside	0.39	0.75	0.25
H2m_oppo	6.25	2	4	Opposite	0.39	0.75	0.25
H2m_oppo_sat	6.25	2	4	Opposite	1	0.75	0.25
H2m_oppo_sat_rough	6.25	2	4	Opposite	1	3	0.25
H2m_oppo_sat_rough_clean	6.25	2	4	Opposite	1	3	0.05
H8m	6.25	8	2	Uniform	0.39	0.75	0.25
H8m_sat	6.25	8	2	Uniform	1	0.75	0.25
H8m_sat_rough	6.25	8	2	Uniform	1	3	0.25
H8m_sat_rough_clean	6.25	8	2	Uniform	1	3	0.05
H8m_besi	6.25	8	2	Beside	0.39	0.75	0.25
H8m_oppo	6.25	8	2	Opposite	0.39	0.75	0.25
H8m_oppo_sat	6.25	8	2	Opposite	1	0.75	0.25
H8m_oppo_sat_rough	6.25	8	2	Opposite	1	3	0.25
H8m_oppo_sat_rough_clean	6.25	8	2	Opposite	1	3	0.05

Note. The different side-wall temperature arrangements are illustrated in Figure 1.

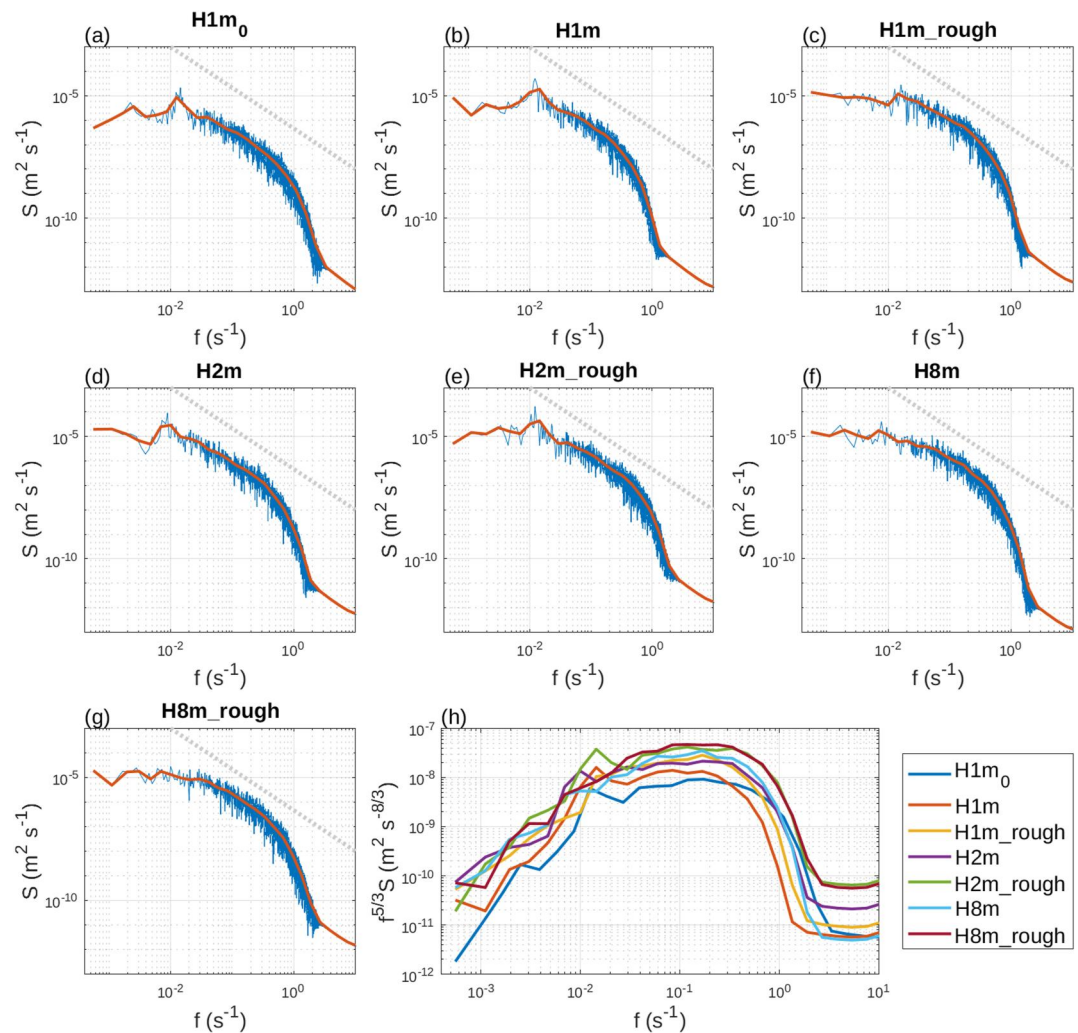


Figure 2. The energy spectra of resolved velocity in each moist simulation measured at the center of the domain with a sampling frequency of 25 Hz (a–g), where the blue line represents the original spectra, the red line represents the logarithmic-bin-averaged data (separated into 30 bins), and the gray dotted line represents the slope of $-5/3$ on a log-log plot. Panel (h) compares the logarithmic-bin-averaged data in panels (a–g) and multiplied by $f^{5/3}$ for the purpose of (i) better estimating the inertial subrange (where the slope is 0 now) and (ii) amplifying the small-scale energy for comparison.

before being complicated by the microphysical models. These results are used to modify the SFM, which is then applied to obtain a continuous relationship between the domain aspect ratio and mean supersaturation. Lastly, the dimensionless parameters are included in Appendix D (Table D1); they are provided for comparison with existing literature.

3.1. LES

Each simulation reaches a quasi-steady state within the first 20 min (see the temporal development in Appendix A), so the results during $t = 30\text{--}60$ min of each simulation are used in the presented analysis. Figure 2 shows the energy spectra computed from the time series of velocity sampled at every time step in the center of the domain. Every configuration produces an energy spectrum that exhibits an inertial subrange characteristic of resolved turbulence (Kolmogorov, 1941). Increasing the grid spacing from 3.125 cm (H1m₀) to 6.25 cm (H1m) narrows the width of the inertial subrange (compare Figures 2a and 2b or blue and red lines in Figure 2h), increasing the energy on the large scales and reducing it on the small scale (A. Wang et al., 2021). A rougher surface always yields higher mean resolved TKE (Table 3). (The “mean” here is slightly different from the “domain average” and is computed by averaging a property over interior grid points at least 6 cm away from the walls. The difference between mean

Table 3

The Moist Simulations' Mean Resolved Turbulence Kinetic Energy, Total Internal Energy (I) and Moisture (M) Flowing In/Out of the Domain Through Each Wall (Calculated by the Sensible and Latent Heat Fluxes) Averaged Over the Quasi-Steady State

Case	Mean TKE ($10^{-3} \text{ m}^2 \text{ s}^{-2}$)	Top I (W)	Bottom I (W)	Side I (W)	Top M (g s^{-1})	Bottom M (g s^{-1})	Side M (g s^{-1})
H1m ₀	7.9	-149.0	200.1	-51.2	-0.120	0.180	-0.060
H1m	6.7	-145.5	187.1	-41.4	-0.118	0.167	-0.048
H1m_rough	11.2	-334.5	431.6	-97.6	-0.276	0.389	-0.114
H2m	13.2	-586.9	789.0	-200.7	-0.469	0.704	-0.234
H2m_rough	19.7	-1,253.2	1,694.4	-444.6	-1.015	1.536	-0.524
H8m	12.4	-78.1	215.9	-138.9	-0.052	0.205	-0.154
H8m_rough	18.4	-175.8	474.6	-298.9	-0.117	0.455	-0.339

and domain-average properties, however, is negligible.) Comparing different domain sizes, larger domains (e.g., H2m and H8m vs. H1m) lead to higher Reynolds numbers (Re) and higher TKE (Table 3). A simplistic view suggests that the resolved TKE is determined by the size of the largest eddies to the first-order approximation. These are primarily controlled by the smallest domain dimension, which is 1 m for H1m and 2 m for H2m and H8m. Given the same grid spacing and surface roughness, it can be expected that the TKE in the H2m and H8m domains is roughly twice that in an H1m domain, as indicated in Table 3. The slightly higher TKE in the H2m domain than that in the H8m domain is possibly due to the higher total input internal energy from the larger bottom area.

The TKE is generated in part by buoyancy stemming from the sensible heat fluxes coming from the bottom, and the turbulent mixing, in turn, increases the near-wall temperature gradient and enhances the sensible heat flux. Table 3 shows that the fluxes with a 6.25-cm grid spacing (H1m) are slightly lower than those with a 3.125-cm grid spacing (H1m₀), possibly owing to the reduced resolved TKE. For both internal energy and moisture, the bottom wall is always a source while the top surface is always a sink. In the simulations listed in Table 3, side walls also work as a net sink. For the H8m domain, the side walls replace the top surface as the main sink owing to their larger area. Rougher surfaces yield higher sensible heat and moisture fluxes and, therefore, the total input internal energy and moisture, as expected. In all cases, the residuals (summing the value of all walls) of the total internal energy and moisture rates during the quasi-steady state are less than 1% of the bottom flux, showing that the simulations exhibit steady-state conditions.

The box chart in Figure 3 shows the spatial and temporal statistics in the entire domain. A simulation using a finer grid spacing (H1m₀) has a similar temperature, water vapor mixing ratio, and supersaturation distribution as the simulation with a coarser grid spacing (H1m). Rough surfaces do not change the mean but produce a wider distribution. Increasing the domain size while keeping the aspect ratio (i.e., going from H1m to H2m) does not change the mean value but slightly reduces the standard deviation (compare H1m_rough with H2m_rough), probably because of more intense mixing as Re increases. As the aspect ratio decreases (i.e., H8m), mean values for all three variables decrease owing to the expanded area of side walls that are colder and drier than the domain mean.

3.2. Using LES-Predicted Wall Fluxes to Modify the Scalar Flux-Budget Model

The SFM (see Section 3 of Thomas et al., 2019), as a simpler model compared to LES, is used to evaluate the results in the moist simulations. In brief, SFM assumes that the tendency of a well-mixed scalar in a closed domain depends on the sum of the fluxes from all surfaces:

$$\frac{\partial}{\partial t}(\bar{\Psi}V_0) = F_bA_b + F_tA_t + F_sA_s, \quad (2)$$

where Ψ is the scalar of interest (e.g., temperature or moisture), the overbar represents the domain average, V_0 is the domain's volume, F_i are the wall fluxes for the scalar, A_i are the wall areas, and the subscripts b , t , and s indicate bottom, top, and side walls, respectively. Thomas et al. (2019) applied two assumptions:

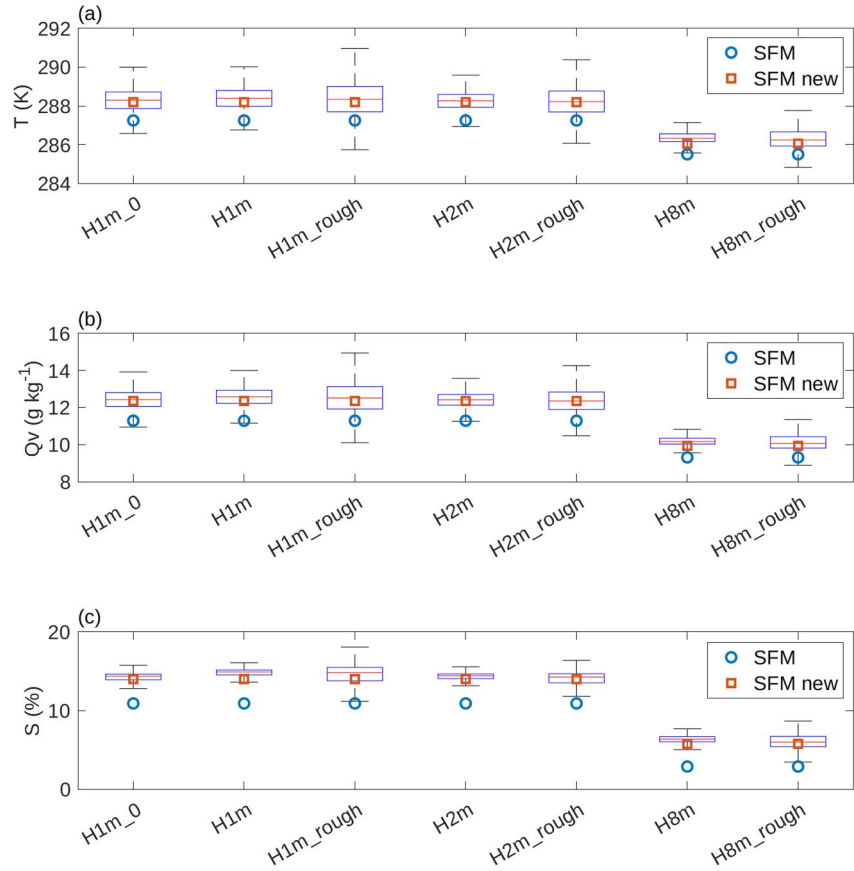


Figure 3. Statistics of temperature, moisture, and supersaturation fields from the large-eddy simulation (LES) moist simulations and mean values predicted by the original (Equation 5, blue circles) and improved (Equation 7, red squares) Scalar Flux-budget Model. The LES statistics are represented by the mean (red lines), 25th to 75th percentiles (boxes), and the most extreme values (whiskers) computed from all grid point values in the entire domain between $t = 30$ min and $t = 60$ min.

$$F_{b/t/s} = C_{b/t/s}(\Psi_{b/t/s} - \bar{\Psi}), \quad (3)$$

$$C_b = C_t = C_s, \quad (4)$$

where C_i are the flux velocities (e.g., Schumann & Moeng, 1991). With the known area ratio, $\hat{A} = A_s/A_b$, and $A_b = A_t$, the steady-state result can be represented as

$$\bar{\Psi} = \frac{\Psi_b + \Psi_t + \hat{A}\Psi_s}{2 + \hat{A}}. \quad (5)$$

The mean temperature and water vapor mixing ratio predicted by Equation 5, as well as resulting supersaturation are plotted as blue circles in Figure 3. All the values predicted by SFM are lower than those obtained by LES. To examine possible reasons for the SFM bias, we use LES to evaluate the SFM representation of the sensible heat flux using Equation 3. Specifically, we evaluate $C_{b/t/s}$ for each wall via

$$C_{b/t/s} = \frac{F_{b/t/s}}{\rho c_p (T_{b/t/s} - \bar{T})}, \quad (6)$$

where the variables on the right-hand side are computed from LES. Here ρ is air density, c_p is specific heat capacity, $T_{b/t/s}$ and \bar{T} are temperatures of the surfaces and mean temperature of air, respectively, and $F_{b/t/s}$ are the mean LES sensible heat fluxes for that surface. Figure 4 shows that the top and bottom walls always have

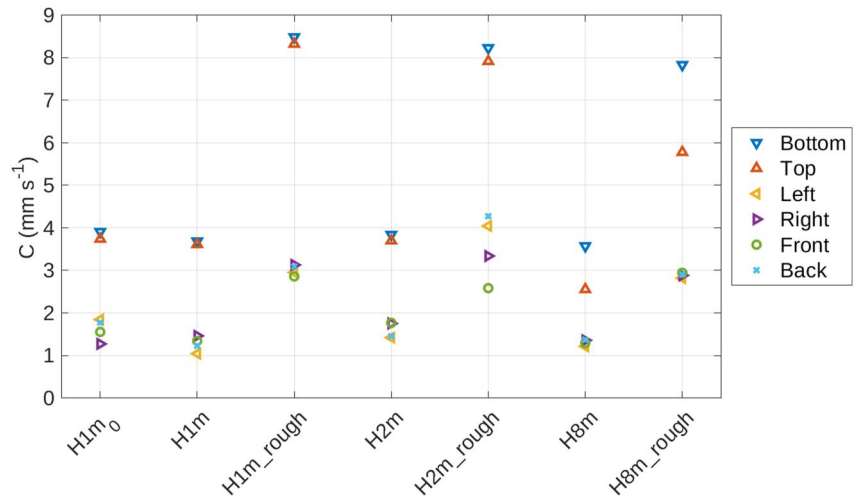


Figure 4. Flux velocities (C) for all walls computed from large-eddy simulation fields using Equation 6. The results are averaged over $t = 30\text{--}60$ min period for the moist simulations listed in Table 1.

significantly higher C than those of the side walls. The reason is the presence of convectively unstable stratification near the top and bottom surfaces, whereas the neutral conditions are applied when fluxes are computed for the side walls. Physically, positive buoyancy (unstable stratification) contributes to the production of turbulence that carries heat flux, and thus results in higher C for top and bottom surfaces.

Figure 4 illustrates that C can vary among the side walls. This is because, due to a large-scale circulation in the chamber, the mean near-wall temperature that drives the LES computed flux deviates from \bar{T} , which represents the chamber-mean temperature and is used in Equation 6. Specifically, when the updraft of a large-scale circulation is near a side wall, the rising warm air from the bottom surface forms a stronger local temperature gradient at that wall. This produces a stronger F_s in LES and a larger C as diagnosed from Equation 6. The effect of large-scale flow on C is further complicated as the direction of the circulation changes over time (Anderson et al., 2021; Niedermeier et al., 2018), as depicted in Figure 5 for the H2m and H2m_rough simulations. These changes are demonstrated through the first-level-mean horizontal velocity components, U_1 and V_1 , (Figure 5a) and the three-dimensional snapshots of vertical velocities (Figures 5b–5e). During the quasi-steady state, an updraft of the large-scale circulation in H2m is more often observed near the right and front wall (as seen in the positive U_1 and negative V_1 in H2m, represented by the blue and light blue lines, in Figure 5a), leading to a higher C on the right and front walls and a lower C on the left and back walls (Figure 4). In a similar manner, for H2m_rough, the updraft is observed primarily on the back and left walls during most of the analyzed period (30–60 min) but occasionally shifts from the left to the right walls (represented by the red and pink lines in Figure 5a). This leads to a highest C on the back wall, followed by the left, right, and front walls (Figure 4).

The presented results indicate that the bias in the mean values predicted by SFM relative to LES can be attributed in part to the difference in C between top and bottom surfaces and side walls (i.e., a violation of the assumption in Equation 4). Because the major difference in C comes from the stability (unstable for top and bottom surfaces and neutral for side walls), we can replace the SFM assumption in Equation 4 with a ratio $\hat{C} = C_s/C_b$. Equation 5 then becomes

$$\bar{\Psi} = \frac{\Psi_b + \Psi_t + \hat{C}\hat{A}\Psi_s}{2 + \hat{C}\hat{A}}. \quad (7)$$

Although \hat{C} clearly varies among simulations with different domain configurations shown in Figure 4, we find that using $\hat{C} = 0.35$ significantly improves the prediction of mean scalar values by the SFM (see the red square markers in Figure 3). It should be noted that this \hat{C} value is based on the LES wall model and the chamber configurations of the moist simulations in this study, and its suitability for application to other scenarios is yet to be investigated.

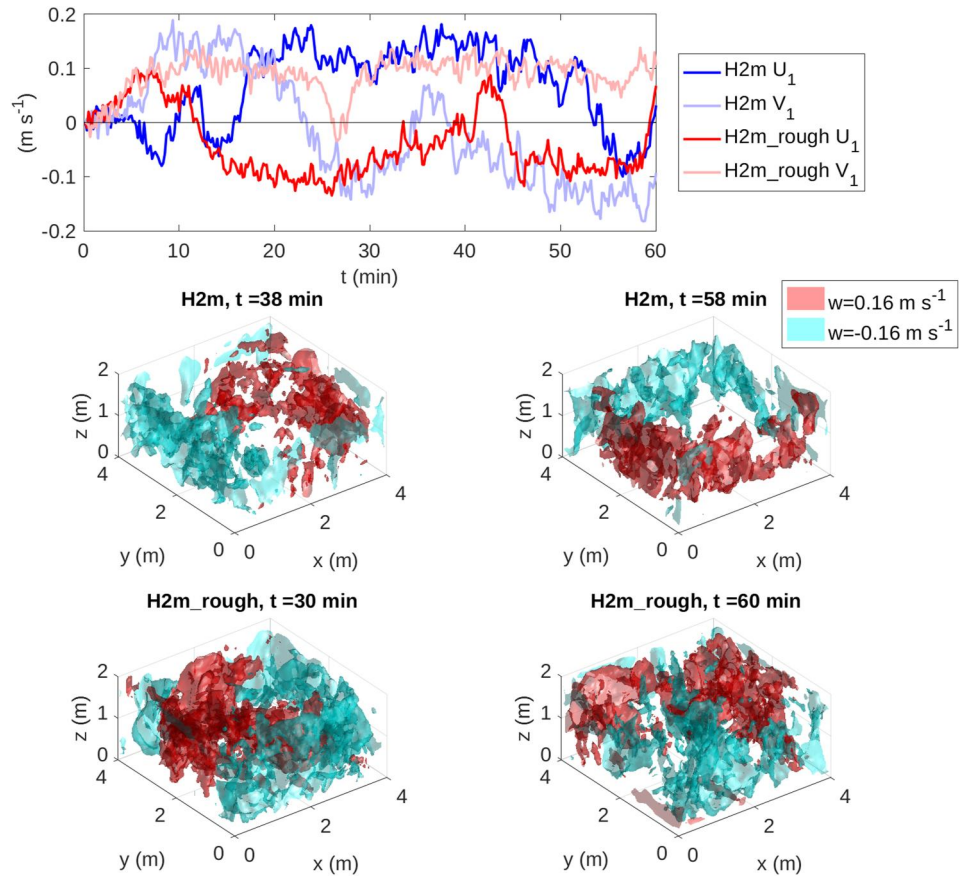


Figure 5. Illustration of the large-scale circulation in the H2m and H2m_rough simulations. Panel a shows the first-level-mean horizontal velocity components (U_1 and V_1). Panels (b–e) present the isosurfaces of updraft (red, $w = 0.16 \text{ m s}^{-1}$) and downdraft (cyan, $w = -0.16 \text{ m s}^{-1}$) at some chosen instances.

The SFM can be used to efficiently explore the effect of various chamber configuration options on the mean state variables, as illustrated by Figure 6, which shows supersaturation as a function of the aspect ratio of the domain. For a given set of top, bottom, and side-wall temperatures and assuming that all surfaces are saturated with respect to liquid water, the mean supersaturation in the chamber is a function of its aspect ratio. The figure shows that the modified SFM (Equation 7 and Figure 6 red line) matches the LES-predicted supersaturation well, while assuming equal flux velocities for horizontal and vertical surfaces (Equation 5) overestimates the effect of side walls and results in an underestimation of supersaturation (Figure 6, blue line). The presence of side walls at a temperature between top and bottom temperatures always reduces the supersaturation in the chamber (as shown in Thomas et al., 2019). Figure 6 quantifies how much this effect is amplified when the aspect ratio of a chamber decreases. For the aspect ratio of 0.25 (cases with the H8m domain in this study), the supersaturation is less than half of that in a chamber with an aspect ratio of 2 (cases with the H1m and H2m domains). It is worth noting that if instead of being at a uniform intermediate temperature, half of the side walls are assigned the bottom temperature and the other half is assigned the top temperature (as in the “besi” and “oppo” arrangements described in Section 2 and Figure 1), then the steady-state solution for a scalar reduces to

$$\bar{\Psi} = \frac{\Psi_b + \Psi_t}{2}, \quad (8)$$

and, therefore, the supersaturation becomes independent of the domain aspect ratio (Figure 6, yellow line). As will be shown below, these non-uniform side-wall temperature configurations produce a significantly higher LWC in the tall chamber.

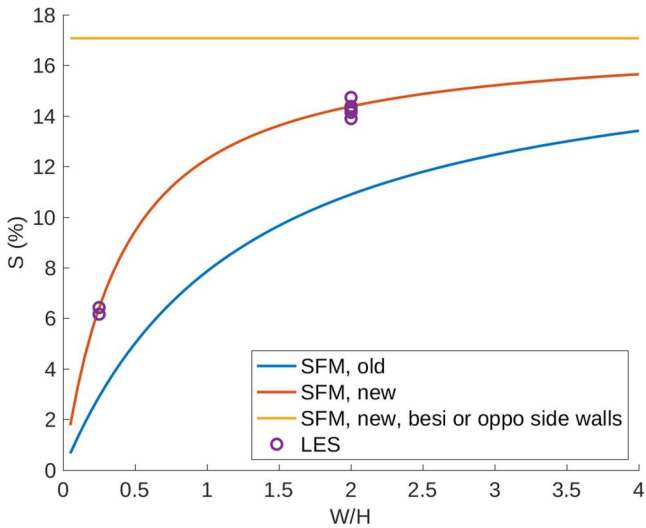


Figure 6. The Scalar Flux-budget Model (SFM) results of supersaturation with saturated walls and different domain aspect ratio (W/H), where W is domain width and H is domain height. The blue line is calculated using the mean temperature and mixing ratio given by Equation 5, the red line is given by Equation 7, and the yellow line is given by Equation 8. \hat{A} used in the SFM (that is, in Equations 5 and 7) is $A_s/A_b = 4HW/W^2 = 4H/W$. The purple circle markers represent the mean values from the 7 large-eddy simulation moist simulations.

4. Results of Cloudy Simulations

In this section, we analyze cloudy LES using model configurations listed in Table 2. Similar to the moist simulations, the scalar fields (represented by relative humidity in Figure A2a) in each simulation reach a quasi-steady state within the first 20 min (Appendix A). The microphysical fields (represented by LWC in Figure A2b) also reach a quasi-steady state at similar time, except for the case H8m_oppo_rough because of the slightly accumulating number concentration, but the conclusion is not affected. Thus, the results during $t = 30\text{--}60$ min of each simulation are still used in the presented analysis. Dimensionless parameters are listed in Table D2 for the readers' information (see Appendix D for details).

Figure 7 shows snapshots of vertical velocity simulated using the H2m and H8m domains and three arrangements of side-wall temperatures: default (uniform), “besi” (the front and left walls as warm as the bottom, and the back and right walls as cold as the top), and “oppo” (the left and right walls as warm as the bottom, and the front and back walls as cold as the top), as shown in Figure 1. In all of these simulations, large-scale flow patterns are clearly visible, in addition to finer and more random turbulent structures. In the simulations with a uniform side-wall temperature, the large-scale circulation can be oriented parallel to walls or along a diagonal, and it can shift throughout the simulation, as was the case with the moist H2m simulation (Figure 5). The large-scale circulation in the H8m simulation with a uniform side-wall temperature can even change direction with height. With the “besi” arrangement, however, the direction of the circulation is oriented along a

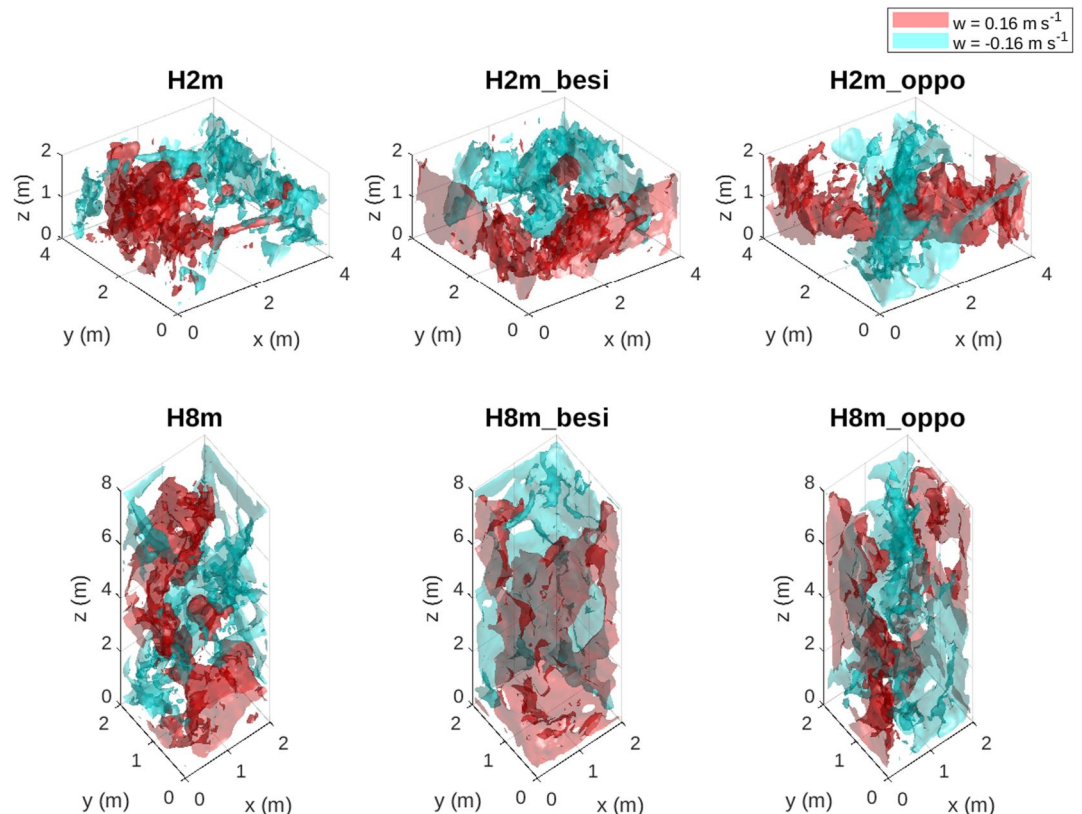


Figure 7. Isosurfaces of positive and negative vertical velocities illustrating large-scale circulations in simulations using two different domains and three arrangements of side-wall temperatures at $t = 60$ min. See Table 2 and text for details.

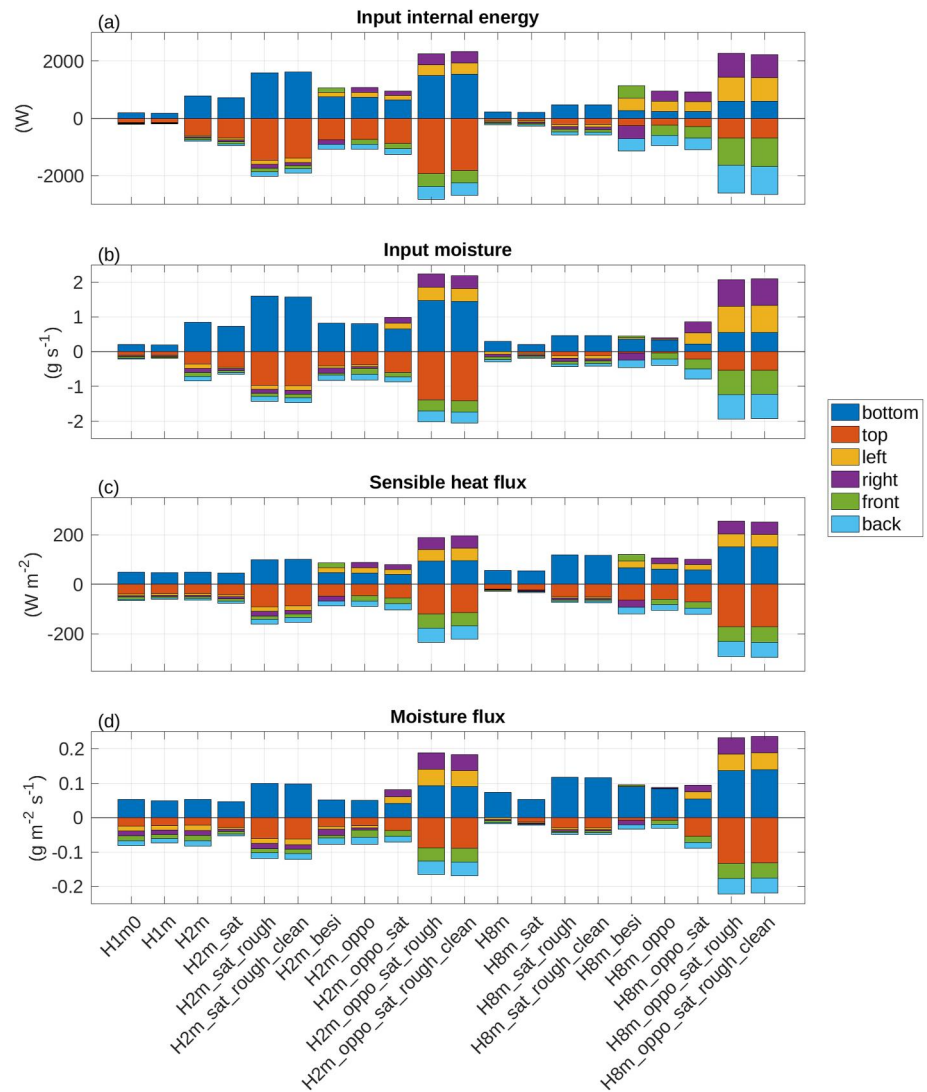


Figure 8. The total input energy (a) and moisture (b) into the domain through each wall and the sensible heat flux (c) and moisture flux (d) on each wall.

diagonal and determined by the side-wall temperature arrangement. Specifically, the updrafts in the “besi” simulations are “attached” to the warmer left and front walls, and the downdrafts are along the colder right and back walls. Using the “oppo” arrangement leads to a more complicated chamber-scale flow pattern. In this case, stronger updrafts and downdrafts appear to be locked not to the opposite corner areas but to the orthogonal diagonal planes. In the middle of the domain, where they intersect, updrafts dominate in the lower half near the warm bottom and downdrafts in the top half near the cold top surface.

Conditions inside a chamber are tightly controlled by the boundary fluxes. In steady-state cloudy conditions, the net moisture influx through the walls is balanced by the loss of water through droplets falling out, and latent heat release from net condensation of water vapor onto the droplets is balanced by the net cooling effect of the walls. Figure 8 shows inputted internal energy and moisture, as well as sensible heat and moisture fluxes, through each wall for all simulations from Table 2 (the values are presented as a Table in Supporting Information S1). Note that the total input of a quantity through a particular wall is equal to the mean flux of that quantity multiplied by the area of that wall.

The comparative analysis, illustrated in Figure 8, shows that increasing the grid spacing from 3.125 to 6.25 cm reduces the fluxes slightly (cf. H1m₀ and H1m), but the effect is small relative to those caused by changes in other

parameters of the model configuration. This supports the use of a coarser grid for the majority of the simulations. Doubling the linear size of the domain, while maintaining the aspect ratio, has little effect on the fluxes (cf. H1m and H2m). However, when the domain size is doubled, the total input of internal energy and moisture nearly quadruples due to the proportional increase in the surface area.

By saturating the side walls, the moisture flux to those surfaces is reduced because of the reduced moisture gradient between the air and the walls in a quasi-steady state (compare H2m_sat to H2m, Figure 8b). At the same time, the heat flux from the bottom is reduced and the flux to the top surface is increased, providing a larger sink of the internal energy, commensurate with the increased net condensation rate (Figure 8a). Making the surfaces rougher boosts the sensible heat and moisture fluxes owing to the enhanced near-wall turbulence (both resolved and subgrid-scale) (compare H2m_sat_rough and H2m_sat). Although the aerosol injection rate influences cloud microphysical properties, which subsequently alters the air temperature and moisture, variations in the aerosol injection rate seem to have relatively small impacts on the wall fluxes (cf. H2m_sat_rough and H2m_sat_rough_clean in Figure 8).

When two side walls are as warm as the bottom, and two others are as cold as the top (i.e., the besi and oppo simulations), the side-wall fluxes increase because of the larger temperature and water vapor mixing ratio gradients between the side walls and the interior domain. Making the side walls saturated under these temperature arrangements increases the contributions of the warm walls to the moisture flux (H2m_oppo_sat vs. H2m_oppo, Figure 8d). Similar to the cases with uniform side-wall temperature, making the surfaces rougher in the besi and oppo cases scales sensible heat and moisture fluxes up for all the walls.

Increasing the height of the chamber and, therefore, reducing its aspect ratio greatly enhances the contributions of the side walls (compare the H2m and H8m series in Figure 8). When the side walls in the H8m domain are held at 285 K, they act together with the top surface as sinks to both internal energy and moisture, while relatively large sensible and latent heat fluxes from the bottom balance these sinks. When the side walls have a non-uniform temperature, although the top and bottom still yield higher sensible heat flux owing to the non-neutral MOST, the side walls become the main source and sink in terms of the total input internal energy. When the side walls are not completely saturated, the bottom is the main source of moisture (H8m_oppo, Figure 8b). When the side walls are saturated, the behavior of the moisture flux and total input moisture is similar to the sensible heat flux and total input internal energy (H8m_oppo_sat, Figure 8). A rougher surface increases the wall fluxes in the H8m and H2m cases (Figures 8c and 8d), but, in the tall chamber, the total internal energy and moisture flow mainly through the side walls (see the rough cases in Figures 8a and 8b), because of their larger area in the H8m compared to the H2m configuration.

In a chamber under steady-state cloudy condition, the net condensation rate must balance the rate of condensate removal by sedimentation. In addition, to keep the internal energy constant, the latent heat released from condensation must be balanced by the net sensible heat sink through the walls. Figure 9 shows that the internal energy balance is indeed well maintained in the analyzed simulations. The figure also illustrates that simulations with saturated side walls lead to much higher net condensation rates in the domain and larger LWCs, as will be shown below.

Having analyzed the wall fluxes, we now turn to the description of the mean dynamical and thermodynamical properties in a chamber. Figure 10a shows that the mean TKE increases with the domain volume owing to the increased Re and with roughness length because of the increased input energy (compare the H1m with the H2m and H8m simulations and recall that the H2m and H8m domains have the same volume). Most of the H8m simulations have slightly lower TKE than H2m simulations, as was also the case with the moist simulations (see Table 3), except for H8m_oppo_sat_rough and H8m_oppo_sat_rough_clean. Figure 10b illustrates that with a uniform side-wall temperature, a larger wall area in the H8m simulations contributes to lowering the mean temperature in the chamber because the wall temperature is below the mean of the top and bottom. Figure 10c shows that the supersaturation (and, therefore, relative humidity) is the highest in the clean cases. The relative humidity is also higher in the H2m than in the H8m simulations, which is related to the differences in steady-state microphysical cloud properties in these two configurations for the same total aerosol injection rate. If the side walls are not completely saturated, a domain larger than H1m cannot maintain a positive mean supersaturation (at least with the baseline wetness of 39% used in this work) (Figure 10c) and only one of these simulations is able to maintain some cloud water (H2m, Figure 10e). Figure 10d shows that the mean water vapor mixing ratio is increased mainly by the presence of saturated side walls and, second, by the non-uniform side-wall temperatures

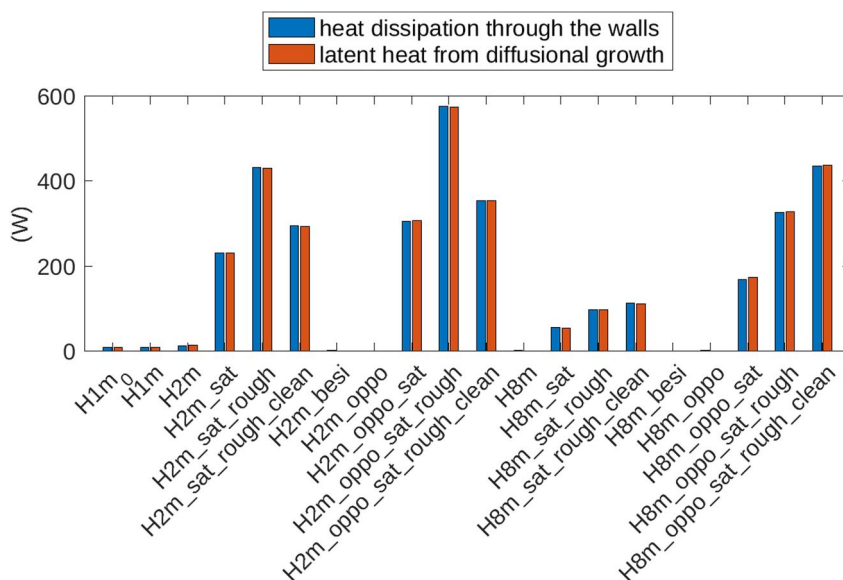


Figure 9. The absolute values of the net energy sink in a chamber domain via sensible heat fluxes through the walls (blue) and the latent heat released from the diffusional growth (red).

(“_oppo_” simulations). Figure 10e indicates that the cloud water is also significantly higher in simulations with saturated side walls. Clean cases, in which the aerosol injection rate and, therefore, cloud droplet number concentration are substantially reduced, exhibit a lower cloud LWC (Figure 10e, consistent with the observation in Thomas et al., 2022). Note that for the H8m domain, the total condensational growth is higher in clean cases (Figure 9), thus the lower LWC results from enhanced sedimentation of larger droplets.

Additional microphysical properties are shown in Figure 11. Figure 11a shows that, when clouds do form in the H8m simulations, they have significantly higher number concentrations than those in the H2m domain for the same injection rate, but cloud formation in the H8m cases only happens when the side walls are saturated. The differences in microphysical properties between the H2m and H8m simulations can be understood by considering the droplet concentration budget. In a steady state, it requires that activation of new droplets is balanced by the removal of existing ones through sedimentation. The two domains have the same volume and, consequently, the same integral aerosol injection rate. The total rate of droplet removal from the chamber volume, however, is proportional to the bottom surface area, which is four times larger in the H2m domain than in the H8m domain. Therefore, a higher droplet concentration in the H8m simulations is required to produce the same droplet removal rate as in H2m simulations. A comparison of Figures 10e, 11a, and 11b suggests that the higher droplet number concentration is the main reason for the higher cloud water content in the H8m domain. The mean droplet size is slightly reduced in the H8m relative to the H2m simulations, except in the oppo_sat_rough_clean case (Figure 11b). The standard deviations of the droplet radius show the same trends as the mean radius (compare Figure 11 panels b and c), such that the relative dispersion of the DSD (i.e., standard deviation divided by mean) is almost independent of the setup.

Figure 11d reveals that the rate of droplet concentration reduction due to collision-coalescence is highly correlated with LWC (Figure 10e), in line with the general theoretical expectations (e.g., Long, 1974; Wood, 2006). The H8m simulations with the oppo_sat configurations have significantly higher collision rates than the corresponding H2m simulations, which have similar (even slightly larger) mean droplet sizes but lower number concentrations. Although the clean case (_H8m_oppo_sat_rough_clean) has the largest mean droplet radius and standard deviation of the DSD, both of which favor collision-coalescence, the decreased number concentration in this case significantly reduces the total number of collisions (Figure 11d). However, the clean case yields the highest collision-coalescence rate per droplet (Figure 11e, which is derived by the values in Figure 11d divided by those in Figure 11a).

Cloud droplet size spectra from the baseline case (H1m) and several other representative model configurations are shown in Figure 12. The higher number concentrations in the H8m simulations compared to the corresponding

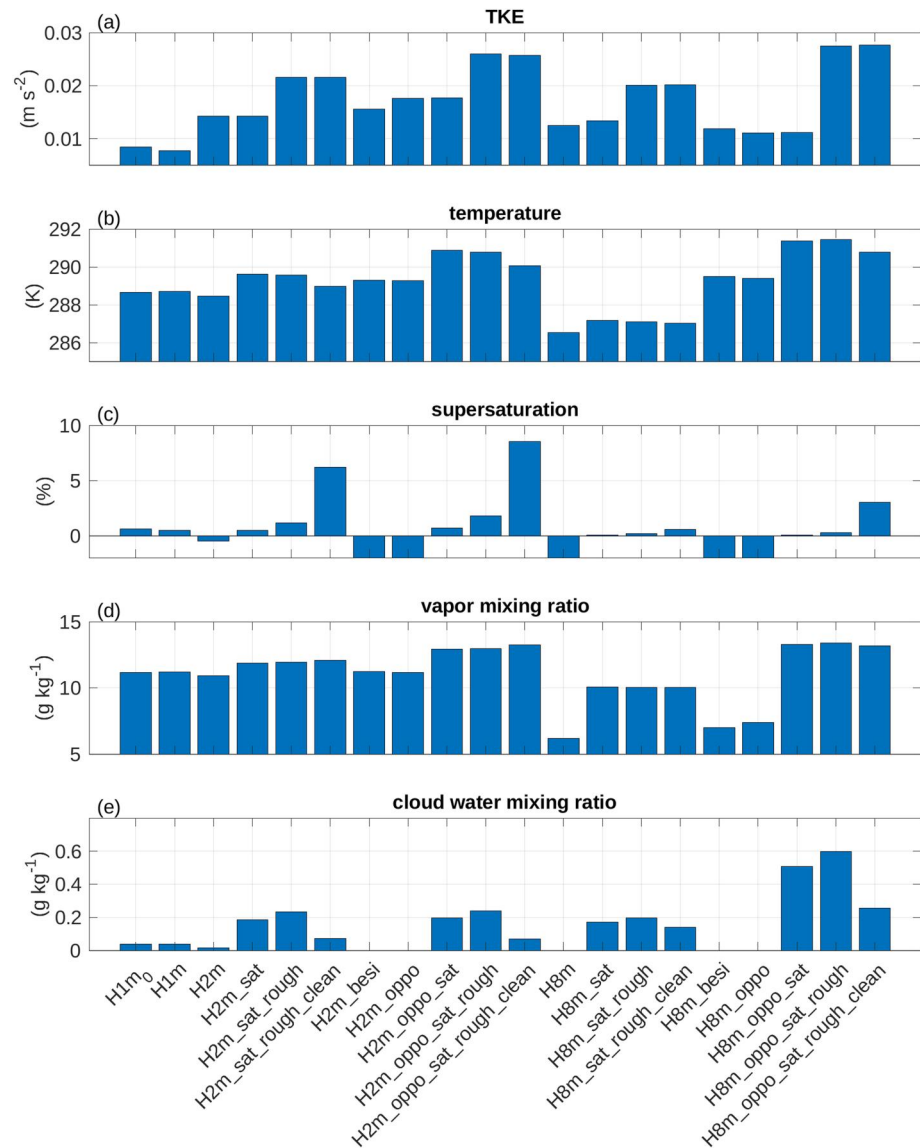


Figure 10. The cloudy simulations' mean (a) turbulence kinetic energy, (b) temperature, (c) supersaturation (the values lower than -2% are not of interest), (d) vapor mixing ratio, and (e) cloud water mixing ratio. The results are averaged over $t = 30\text{--}60$ min.

H2m simulations are again revealed through a comparison of the red and blue lines in Figures 12a and 12b. When the DSDs are normalized by total droplet concentration and presented as a probability density function, changes in the modal radius, spectral width, and, more generally, in the shape of the spectra can be visually compared (Figures 12c and 12d). By applying a non-uniform side-wall temperature and increasing the surface roughness, broader droplet spectra with a larger modal radius can be obtained in both H2m and H8m chamber geometries. The changes in the DSDs are larger for the tall (H8m) domain because of the higher rate of collision-coalescence (Figure 12e).

Analysis of the DSDs can identify conditions that favor the formation of broader DSDs but cannot clearly separate relative contributions of collision-coalescence and other processes contributing to spectral broadening (e.g., diffusional growth in a fluctuating supersaturation field is also known to contribute to spectral broadening). To better quantify the effect of collision-coalescence, five cases are repeated with collision-coalescence calculations turned off (these are indicated by “_nocoll” appended to the case names). The DSDs from simulations with and without collision-coalescence are compared in Figure 13. Among these experiments, the strongest impact of

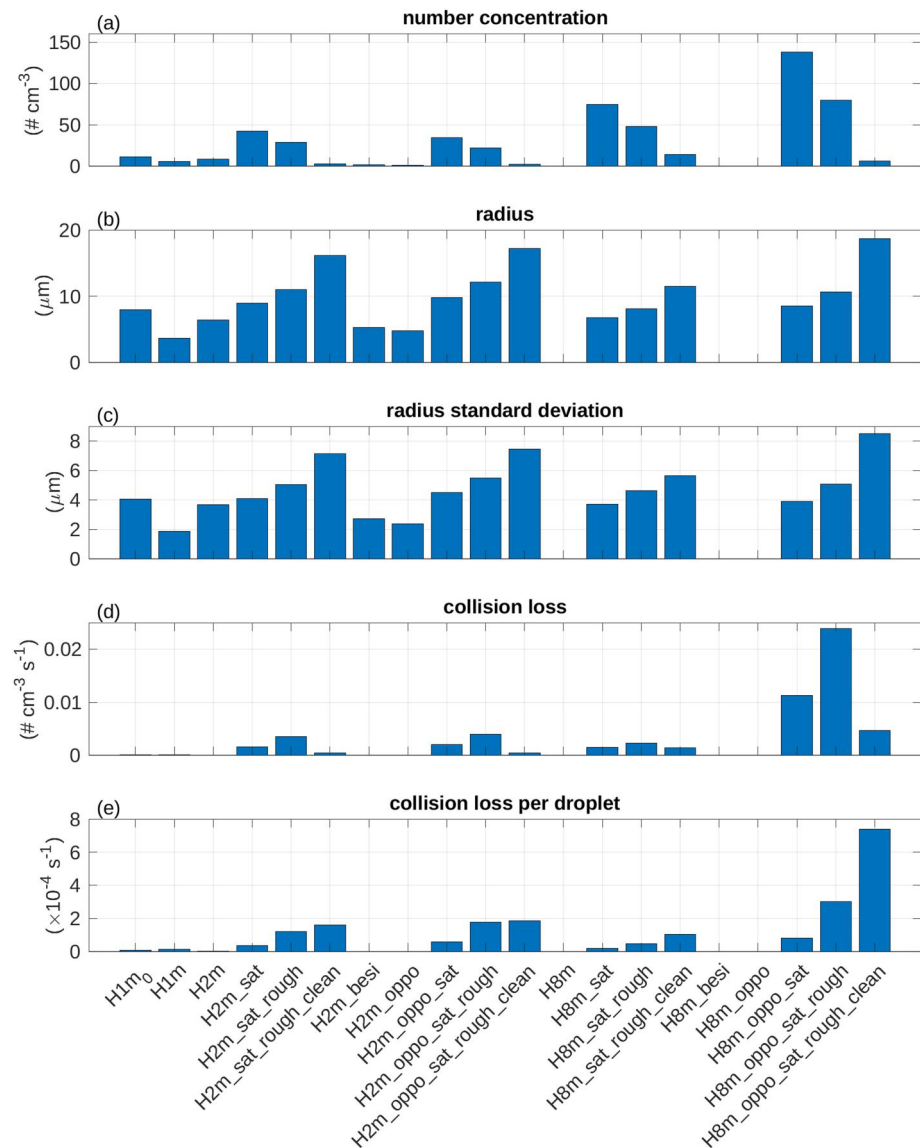


Figure 11. The cloudy simulations' mean (a) number concentration of cloud droplet, (b) droplet radius, (c) droplet radius standard deviation, (d) domain-average collision loss, and (e) collision loss per droplet. The results are averaged over $t = 30$ – 60 min.

collisions on the DSD is found in the H8m_oppo_sat_rough setup, in which collision-coalescence reduces the number concentration of droplets roughly smaller than $20 \mu\text{m}$ in radius and increases the number concentration of the large droplets (compare the red and blue dashed lines in Figure 13). Interestingly, the broadest droplet size spectrum in H8m_oppo_sat_rough_clean appears to be affected very little by collisions (compare the red and blue dotted lines in Figure 13) despite having the highest per-droplet collision rate (Figure 12e). This can presumably be attributed to the lower total droplet number concentration, which reduces the frequency of collision-coalescence, and the shortened in-chamber residence time of larger droplets, which further diminishes the chances of collision-coalescence.

5. Conclusions and Discussions

Collision-coalescence has been identified as an important process in cloud physics that is very challenging to be quantitatively studied using current laboratory facilities (Shaw et al., 2020). Recently, Thomas et al. (2023)

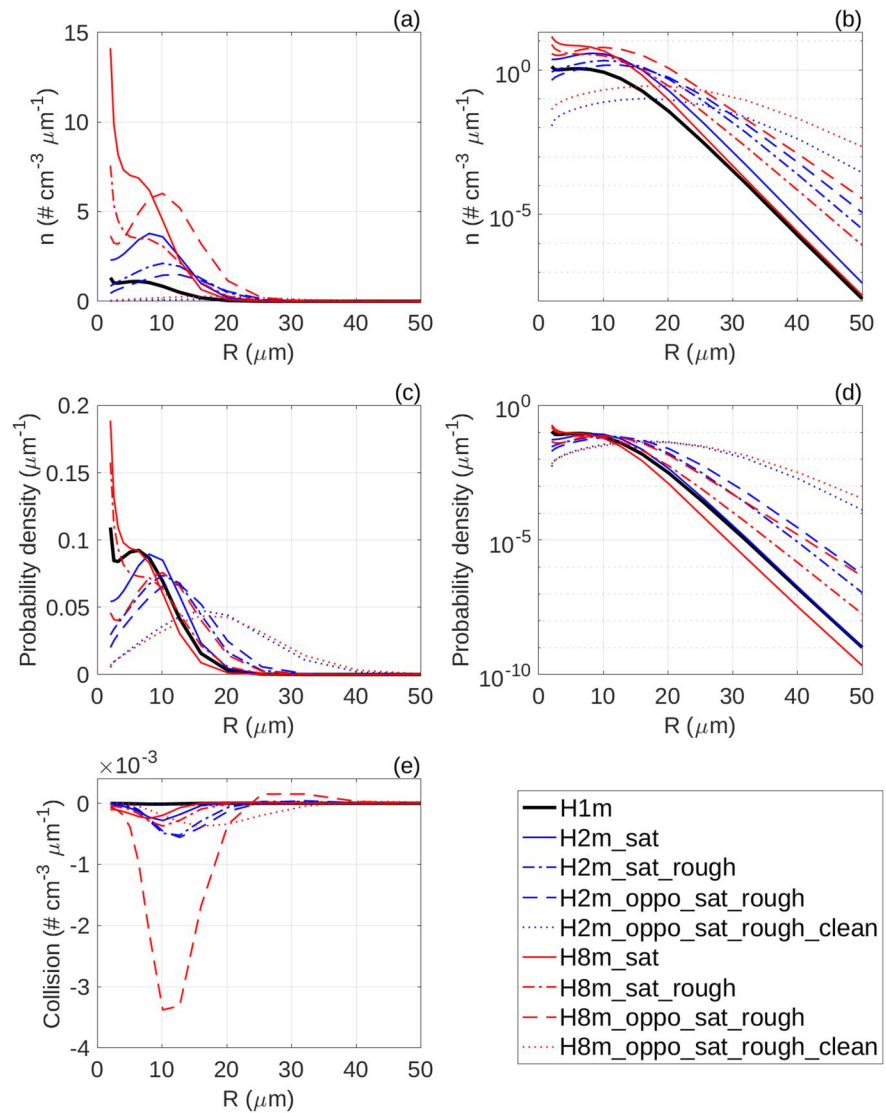


Figure 12. Droplet size distributions from selected simulations represented by number concentration density using linear and log scale (a, b, respectively). (c, d) The same as panels (a, b) but normalized by the total number concentration. Also shown is the spectral distribution of the rate of change of droplet size distribution (DSD) due to collision-coalescence (e). The results are averaged over the interior of the chamber and over the 30–60 min time window.

demonstrated that the effects of droplet collisions on DSDs could be potentially investigated in a scaled-up version of a convection-cloud chamber, known as a Pi-Chamber, currently operated at the Michigan Technological University (Chang et al., 2016). Following up and expanding the study by Thomas et al. (2023), this work uses numerical modeling to explore the effects of various cloud chamber setup parameters on steady-state cloud properties, including the DSDs and the degree to which they are influenced by the collision-coalescence process. The investigated parameter space includes domain size, domain aspect ratio, side-wall temperature and wetness, surface roughness, and aerosol injection rate. Numerical simulations are performed using SAM LES with a bin microphysics scheme, which was previously applied to Pi-Chamber modeling (Chandrakar et al., 2016; Thomas et al., 2019, 2023; Yang et al., 2022), but with several modifications and improvements to the treatment of the cloud chamber walls.

Moist simulations, that is, simulations without condensation and evaporation within the domain, are first performed to explore characteristics of turbulence inside a convection chamber, sensible and latent heat fluxes at the

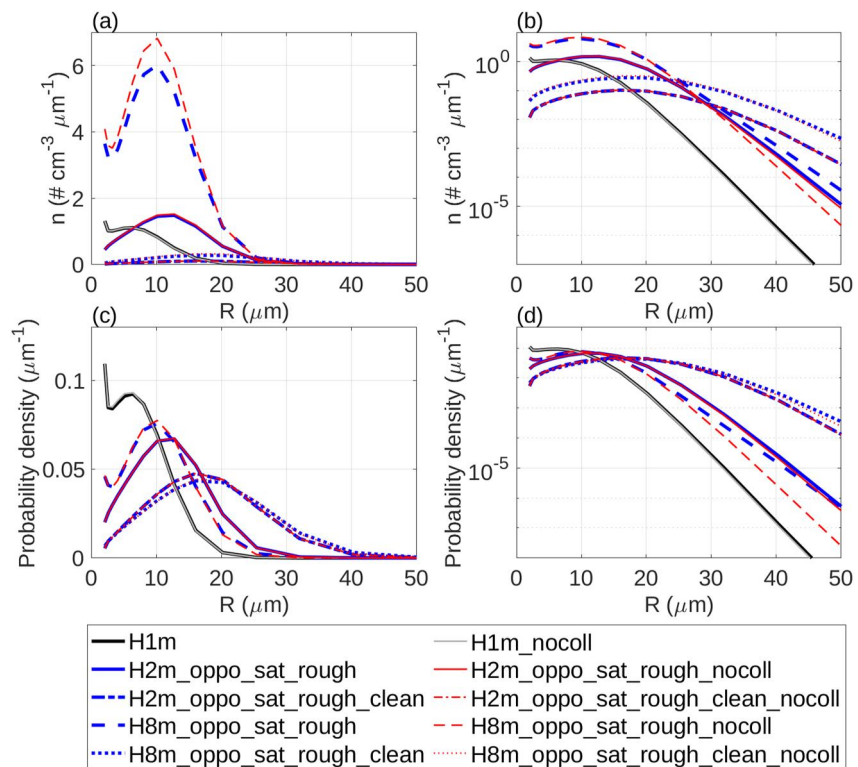


Figure 13. Similar to Figures 12a–12d but with five chosen cases compared to those using the same configurations except turning off collision scheme (with “_nocoll” appended to the case names).

walls, and attainable supersaturation. Analysis of the velocity power spectra demonstrates that these simulations resolve an inertial subrange, which confirms the suitability of the LES approach. The analysis of the LES-predicted sensible heat and moisture fluxes for all the walls reveals that the fluxes to/from the top and bottom surfaces are larger than those on the side walls because of the significant contribution from the buoyancy-generated turbulence near the top and bottom, where the temperature profile is highly unstable. Fluxes at the side walls lack this direct contribution from buoyancy. This finding is used to modify an assumption of SFM that the flux coefficient relating the scalar flux to the scalar difference between the mean value in the chamber and the value at the wall is the same for all walls. With a reduced flux coefficient for the side walls (compared to that of the top and bottom), the SFM can reproduce the supersaturation obtained in the LES. However, it should be noted that the SFM modification is based on the assumption that MOST generally outperforms an assumption of constant flux velocity for the entire domain, despite the limitations of MOST. On the application of the SFM, it allows us to compute the mean supersaturation continuously over a wide range of possible aspect ratios for the chamber. This exercise highlights the need for non-uniform side-wall temperature in the case of a low aspect ratio or the tall chamber configuration considered in Figure 1a.

Cloudy simulations with a size-resolved (bin) microphysics scheme are performed to explore the effects of various chamber configuration options on the droplet collision rate. The results show that saturated side walls (or, at least a much higher wetness than 39%) are necessary to maintain a cloud. Alternatively, the side walls reduce the mean supersaturation to below zero in all tested domains larger than that of the Pi Chamber. Implementing water-saturated side walls in the modeled chamber provides the largest increase to the domain mean LWC (Figure 10e), which is one of the main factors controlling the collision rate.

Using rougher surfaces increases the wall fluxes and provides an additional boost to the attainable LWC in all chamber geometries. For the tall chamber (H8m), switching to non-uniform wall temperatures, with two walls at the temperature of the bottom and two at the temperature of the top, results in more than doubling the domain mean LWC relative to the cases with a uniform intermediate side-wall temperature (Figure 10e).

Reducing the aerosol injection rate broadens the DSDs, as has been shown previously (e.g., Chandrakar et al., 2016), and, therefore, increases the per-droplet collision rate (Figure 11e). At the same time, a lower aerosol injection rate leads to a reduction in droplet number concentration (Figure 11a) and LWC (Figure 10e), and consequently to a smaller collision rate (Figure 11d), which is well correlated with LWC, consistent with theoretical predictions (e.g., Long, 1974; Wood, 2006). Simulations performed with and without the collision-coalescence process show that the presence of a broad droplet spectrum does not necessarily imply that this DSD is significantly impacted by droplet collisions.

The presented study identifies some key aspects of a convection-cloud chamber configuration that would promote the collision-coalescence process and make it possible to study it quantitatively in a controlled laboratory environment. This work also demonstrates the practical utility of numerical modeling in designing an optimal experimental setup for enhancing the effects of collisions on DSDs. Although the effects and sensitivities discussed here are meaningful, additional efforts are underway to improve the accuracy of the models and conduct a more systematic exploration of the parameter space. In particular, significant attention is given to the evaluation of the representation of surface fluxes in LES using both observations in the Pi chamber and advanced modeling approaches. Although direct measurement of scalar and momentum fluxes in the Pi Chamber is challenging, the sensitivity of the thermodynamics and cloud properties in the chamber to surface characteristics, such as surface roughness, can provide a target for model evaluation.

To keep our readers aware of the challenges and uncertainties inherent in modeling wall fluxes, here we briefly discuss some preliminary results from two recent activities in this area. The first study, aiming to evaluate and improve surface fluxes in LES, involves an intercomparison of different wall models in LES and DNS. Preliminary findings suggest that, while adjusting the roughness lengths in the law of the wall or MOST can bring the mean surface fluxes in LES close to those from DNS, the roughness length selected for the top and bottom may not be appropriate for the side walls. Additionally, the law of the wall might outperform MOST when the side-wall temperature is uniform, but it underperforms when the side-wall temperature becomes non-uniform. Multiple factors could lead to such discrepancies, including under-resolved corner regions. Results from this study will be documented in future publication. The second study is recently published (A. Wang et al., 2023). It reveals that, in simulations of the Rayleigh-Bénard convection, the MOST-based parameterization does not capture local details accurately, leading us to explore an alternative approach using machine learning techniques.

Finally, it is important to acknowledge that, while the primary goal of this work is to examine factors that can enhance collision-coalescence in a cloud chamber, the collision-coalescence model used in bin microphysics may not be entirely accurate. Hill et al. (2023) demonstrated that the DSDs in warm rain processes are sensitive to the selection of the collision-coalescence model. Although testing the sensitivity of simulated cloud properties to the collision-coalescence model could be a valuable direction for future research, in this study we focus on trends in the LWC and collision-coalescence rate in response to changes in chamber configuration. Uncertainties in collisional growth of droplets, however, highlight the importance and urgency of building a cloud chamber for studying collision-coalescence, which is the main motivation behind this study.

Appendix A: Temporal Evolution of the Mean Flow Quantities

To examine the achievement of quasi-steady states, we analyze the time series of mean flow quantities in each simulation. For the moist simulations, the dynamic fields, represented by turbulence kinetic energy (TKE), reach quasi-steady states within 10 min (Figure A1b). The scalar fields, represented by relative humidity, also reach quasi-steady states within 10 min for the H1m and H2m simulations, and within 20 min for the H8m simulations because of the lower relative humidity they need to achieve (Figure A1a). For the cloudy simulations, most scalar fields reach quasi-steady state within 10 min (Figure A2a), with the exception of the H8m simulations without saturated side walls, due to the low relative humidity they need to achieve. In addition, most microphysical fields, represented by liquid water content (LWC), reach quasi-steady states within 10 min (Figure A2b), except for H8m_oppo_sat and H8m_oppo_sat_rough. For H8m_oppo_sat_rough, the delay is due to the high LWC it needs to reach. For H8m_oppo_sat, the LWC continues to slightly increase even after 20 min due to the increase in number concentration, which results from the accumulation of aerosols. Despite the slight increases in number concentration and LWC, the conclusions of this study are not affected.

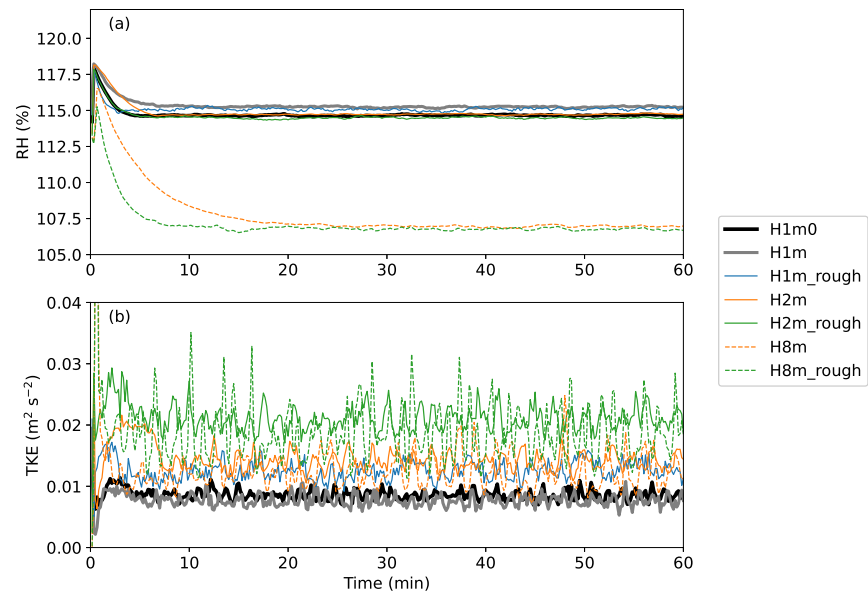


Figure A1. The time series of (a) relative humidity (representing the scalar fields) and (b) turbulence kinetic energy (representing the dynamic fields) of the moist simulations.

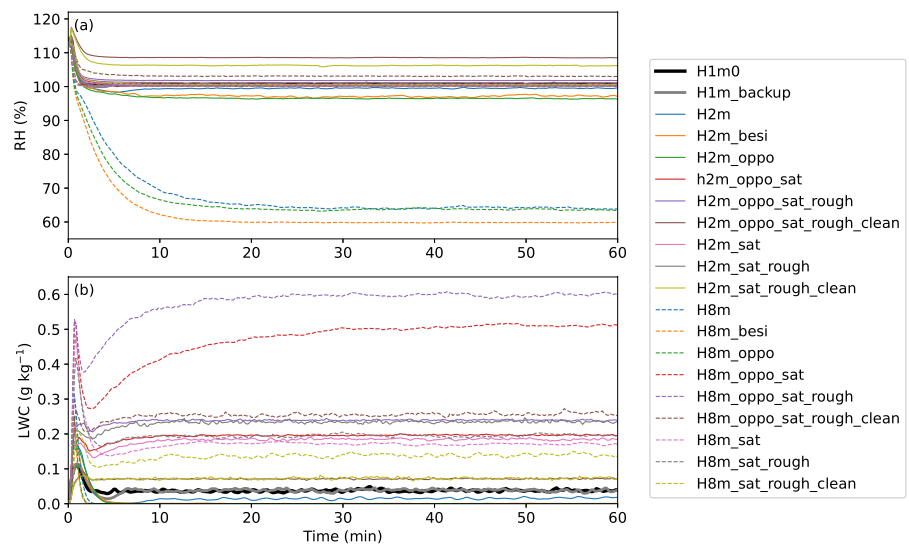


Figure A2. The time series of (a) relative humidity (representing the scalar fields) and (b) liquid water content (representing the microphysical fields) of the cloudy simulations.

Appendix B: Determining the Roughness Length

Currently, there is no reliable method to accurately measure the surface fluxes in the real Pi Chamber. Previous large-eddy simulation (LES) of the Pi Chamber determined the z_0 by approximately matching the standard deviation of the vertical velocity to 0.1 m s^{-1} (Thomas et al., 2019). Recently, Chandrakar et al. (2022) obtained direct numerical simulations (DNS) data for a similar domain and flow pattern, showing good agreement with the Pi Chamber's near-wall temperature and water vapor standard deviations. As such, we utilize this accurate DNS flux data to determine z_0 for LES. Following Chandrakar et al. (2022), our LES domain here is $(1 \text{ m})^3$, with top, bottom, and side-wall temperatures set at 282, 294, and 288 K, respectively. The side walls, like the top and bottom walls, are saturated. We test two SGS models (Smagorinsky and 1.5-order TKE) and two grid spacings (3.125 and 6.25 cm).

We determine the roughness length, z_0 , by aligning the Nusselt (Nu) and Sherwood (Sh) numbers obtained from various LESs with those from the DNSs. The Nu and Sh numbers are defined as follows:

$$Nu = \frac{F_T H}{k \Delta T}, \quad (B1)$$

$$Sh = \frac{F_q H}{D \Delta q}. \quad (B2)$$

Here, F_T represents the sensible heat flux (W m^{-2}); H is the domain height (m); $k = 0.024 \text{ W m}^{-1} \text{ K}^{-1}$ represents the thermal conductivity of air; ΔT refers to the bottom-top temperature difference (K); F_q denotes the moisture flux ($\text{g kg}^{-1} \text{ m s}^{-1}$); $D = 2.21 \times 10^{-5} \text{ m}^2 \text{ s}^{-1}$ is the diffusivity of water vapor; and Δq represents the bottom-top moisture difference (g kg^{-1}).

For saturated side walls as illustrated in Chandrakar et al. (2022) (refer to their Figure 2, Case 2), Nu for the bottom and top walls are approximately 73 and 75, respectively, and the Sh numbers are around 77 and 64. Based on the LES results, we infer that z_0 should lie between 0.7 and 0.8 mm (see Figure B1), so we select $z_0 = 0.75 \text{ mm}$ for our baseline simulation. As illustrated in Figure B1, the LES results are not sensitive to the variations in the SGS models and grid spacings.

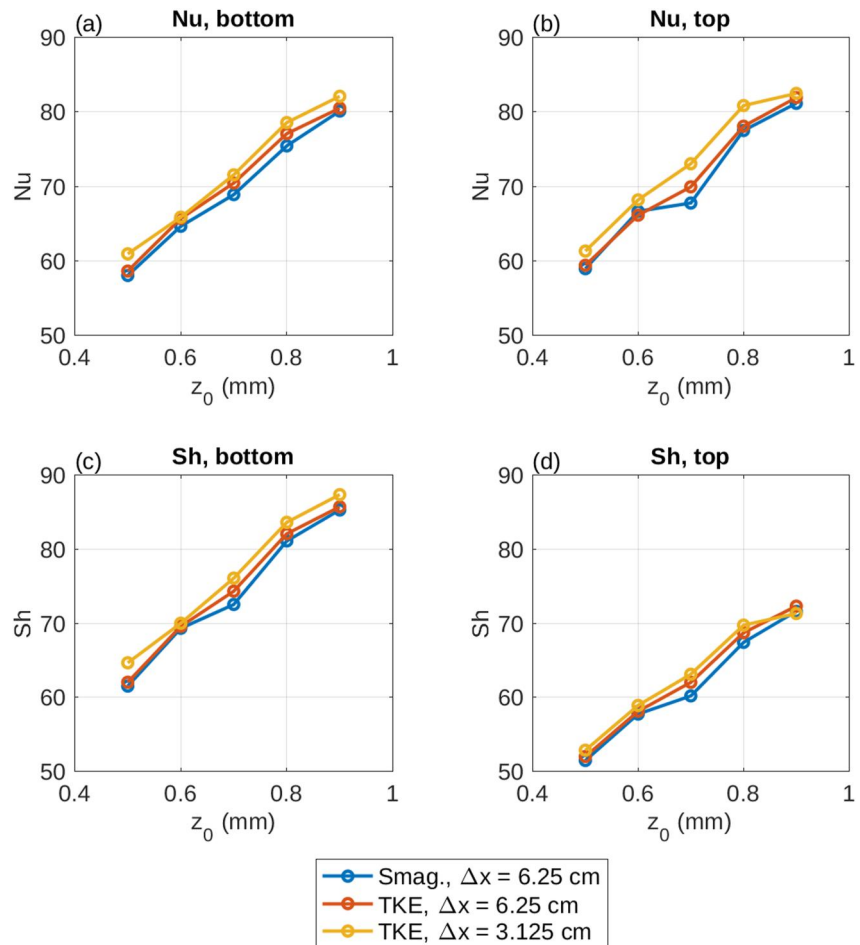


Figure B1. The large-eddy simulation results of Nusselt number (a, b) and Sherwood number (c, d) employing different z_0 , subgrid-scale models, and grid spacings, using the domain size and side-wall temperature following Chandrakar et al. (2022) with saturated side walls.

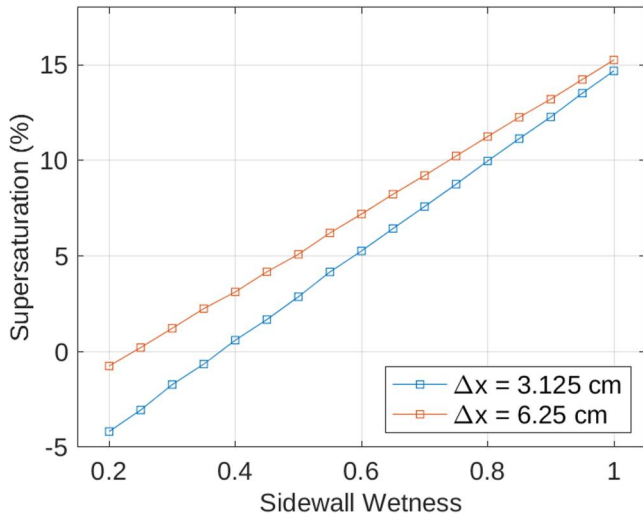


Figure C1. The large-eddy simulation results of supersaturation employing different side-wall wetnesses and grid spacings using the domain size and side-wall temperature following Thomas et al. (2019) with $z_0 = 0.75$ mm (as specified in Appendix B).

Appendix C: Determining the Side-Wall Wetness

Using the z_0 specified in Appendix B, we performed LESs with varying degrees of side-wall wetness to match the observed supersaturation of 2.5% in the Pi Chamber. The computational domain size is identical to that of the Pi Chamber, being $2 \text{ m} \times 2 \text{ m} \times 1 \text{ m}$, and the top, bottom, and side-wall temperatures are set to 280, 299, and 285 K, respectively, in accordance with Thomas et al. (2019). The mean supersaturation is computed in the interior domain, defined as the region more than 6.25 cm away from the walls.

As illustrated in Figure C1, there exists a linear relationship between supersaturation and sidewall wetness. Therefore, the wetness for the baseline LESs in this study is determined by linear interpolation between the two tested wetnesses to achieve a supersaturation of 2.5%. Because the results are sensitive to grid spacing, we apply side-wall wetnesses of 0.39 and 0.50 for the simulations with 6.25- and 3.125-cm grid spacings, respectively, when the side walls are not fully saturated (see Table 2).

With a fixed side-wall wetness, a coarser grid spacing can result in higher supersaturation due to the potential underestimation of moisture flux, given that the side walls act as moisture sinks. This phenomenon is highlighted by the reduced deviation in the supersaturation obtained from different grid spacings as the side-wall wetness increases.

Appendix D: Dimensionless Parameters

To compare the extensive simulations in this study with the literature, we provide the dimensionless parameters calculated from the mean flow quantities. However, one should bear in mind that the results presented here are influenced by factors such as the wall function, microphysics model, and the wetness and temperatures of the side-walls.

The results of the moist simulations are displayed in Table D1, and the results of the cloudy simulations are in Table D2. In the tables, the Rayleigh number (Ra) is calculated as

$$\text{Ra} = \frac{\beta g \Delta T H^3}{\nu \alpha}, \quad (\text{D1})$$

where β is the thermal expansion coefficient of air, g is the gravitational acceleration, and α is the thermal diffusivity. Nu is calculated as in Equation B1. Because of the different domain aspect ratios tested in this study, the Reynolds number (Re) is calculated based on both the domain height (H) and the geometric mean of domain width ($L = \sqrt[3]{V}$, where V is the domain volume):

$$\text{Re}_H = \frac{\sqrt{EH}}{\nu}, \quad (\text{D2})$$

$$\text{Re}_L = \frac{\sqrt{EL}}{\nu}, \quad (\text{D3})$$

where E is the resolved TKE, equivalent to the resolved kinetic energy in this study.

Table D1
The Dimensionless Parameters of the Moist Simulations

	Ra ($\times 10^9$)	Nu ($\times 10^2$)	Re _H ($\times 10^4$)	Re _L ($\times 10^4$)
H1m0	2.2	1.10	0.64	1.02
H1m	2.2	1.03	0.61	0.96
H1m_rough	2.2	2.37	0.79	1.25
H2m	17.6	2.16	1.65	2.62
H2m_rough	17.6	4.64	2.01	3.20
H8m	1,128.9	9.47	6.25	2.48
H8m_rough	1,128.9	20.82	7.61	3.02

Note. The Nu here, following Equation B1, is calculated from the bottom-wall heat flux. The Ra, Re_H, and Re_L are calculated as Equations D1–D3.

For the cloudy simulations, the Damköhler number (Da) can be derived from the turbulence correlation time (τ_t) and the cloud phase relaxation time (τ_c). Similar to Re, the turbulence correlation time can be evaluated by both H and L , so here we provide two Da for comparison:

$$Da_H = \frac{\tau_{t,H}}{t_c}, \quad (D4)$$

$$Da_L = \frac{\tau_{t,L}}{t_c}, \quad (D5)$$

Table D2
Similar to Table D1, But This Table is for the Cloudy Simulations and Thus Includes Da_H and Da_L, Which Are Calculated as Equations D4 and D5

	Ra ($\times 10^9$)	Nu ($\times 10^2$)	Re _H ($\times 10^4$)	Re _L ($\times 10^4$)	Da _H	Da _L
H1m ₀	2.2	1.09	0.64	1.01	0.16	0.25
H1m	2.2	1.01	0.61	0.97	0.04	0.06
H2m	17.6	2.16	1.66	2.64	0.15	0.23
H2m_sat	17.6	1.98	1.66	2.64	1.04	1.66
H2m_sat_rough	17.6	4.35	2.04	3.25	0.71	1.12
H2m_sat_rough_clean	17.6	4.44	2.05	3.25	0.10	0.15
H2m_besi	17.6	2.06	1.74	2.76	0.02	0.04
H2m_oppo	17.6	2.00	1.85	2.93	0.01	0.02
H2m_oppo_sat	17.6	1.75	1.85	2.94	0.83	1.32
H2m_oppo_sat_rough	17.6	4.08	2.24	3.56	0.55	0.87
H2m_oppo_sat_rough_clean	17.6	4.21	2.23	3.54	0.08	0.12
H8m	1,128.9	9.76	6.22	2.47	0.00	0.00
H8m_sat	1,128.9	9.46	6.44	2.55	5.79	2.30
H8m_sat_rough	1,128.9	20.84	7.89	3.13	3.62	1.44
H8m_sat_rough_clean	1,128.9	20.60	7.90	3.14	1.49	0.59
H8m_besi	1,128.9	11.63	6.07	2.41	0.00	0.00
H8m_oppo	1,128.9	10.89	5.85	2.32	0.00	0.00
H8m_oppo_sat	1,128.9	10.30	5.87	2.33	14.65	5.81
H8m_oppo_sat_rough	1,128.9	26.47	9.23	3.66	6.73	2.67
H8m_oppo_sat_rough_clean	1,128.9	26.53	9.26	3.67	0.94	0.37

where

$$\tau_{t,H} = \frac{H}{\sqrt{E}}, \quad (D6)$$

$$\tau_{t,L} = \frac{L}{\sqrt{E}}, \quad (D7)$$

and

$$\tau_c = \frac{1}{4\pi nrD}, \quad (D8)$$

where n is the droplet number concentration, r is the droplet radius, and D is the modified vapor diffusivity (Kumar et al., 2013, assuming that the variation of D with temperature is small).

Data Availability Statement

The SAM model was kindly provided by Prof. Marat Khairoutdinov and publicly available at <http://rossby.msrc.sunysb.edu/~marat/SAM.html>. The output from the SAM simulations is stored on NERSC HPSS storage system at <https://portal.nersc.gov/archive/home/w/wang1202/www/Wang2023JAMES>.

Acknowledgments

This research is supported by the U.S. Department of Energy Office of Science Atmospheric System Research (ASR) project at PNNL. PNNL is operated for the Department of Energy by Battelle Memorial Institute under Contract DE-AC05-76 RL01830. F. Yang has been funded by the Department of Energy (DOE) as part of the Atmospheric System Research (ASR) program under contract DE-SC0012704. R. Shaw has been funded by the National Science Foundation (NSF) Grant AGS-2133229. This research used resources of the National Energy Research Scientific Computing Center (NERSC), a U.S. Department of Energy Office of Science User Facility located at Lawrence Berkeley National Laboratory, operated under Contract No. DE-AC02-05CH11231 using NERSC awards BER-ERCAP0021333 and BER-ERCAP0024023. We acknowledge Kamal Kant Chandrakar and Xiang I. A. Yang for their contributions to the ongoing works mentioned in the Conclusions and Discussions section. We acknowledge helpful, early discussions with Prasanth Prabhakaran about using surface roughness as a method to obtain higher LWC in a convection-cloud chamber. Lastly, for transparency and following the position statement of the Committee on Publication Ethics (COPE), we acknowledge the assistance of ChatGPT in generating the first draft of data processing code, checking spelling, correcting grammar, along with some refinements for context.

References

- Anderson, J. C., Thomas, S., Prabhakaran, P., Shaw, R. A., & Cantrell, W. (2021). Effects of the large-scale circulation on temperature and water vapor distributions in the π chamber. *Atmospheric Measurement Techniques*, 14(8), 5473–5485. <https://doi.org/10.5194/amt-14-5473-2021>
- Beard, K. V., & Ochs, H. T. (1995). Collisions between small precipitation drops. part ii: Formulas for coalescence, temporary coalescence, and satellites. *Journal of the Atmospheric Sciences*, 52(22), 3977–3996. [https://doi.org/10.1175/1520-0469\(1995\)052\(3977:CBSPDP\)2.0.CO;2](https://doi.org/10.1175/1520-0469(1995)052(3977:CBSPDP)2.0.CO;2)
- Blyth, A. M. (1993). Entrainment in cumulus clouds. *Journal of Applied Meteorology and Climatology*, 32(4), 626–641. [https://doi.org/10.1175/1520-0450\(1993\)032\(0626:EICC\)2.0.CO;2](https://doi.org/10.1175/1520-0450(1993)032(0626:EICC)2.0.CO;2)
- Brooks, H. E., Doswell, C. A., & Cooper, J. (1994). On the environments of tornadic and nontornadic mesocyclones. *Weather and Forecasting*, 9(4), 606–618. [https://doi.org/10.1175/1520-0434\(1994\)009\(0606:OTEOTA\)2.0.CO;2](https://doi.org/10.1175/1520-0434(1994)009(0606:OTEOTA)2.0.CO;2)
- Brooks, H. E., Doswell, C. A., & Wilhelmson, R. B. (1994). The role of midtropospheric winds in the evolution and maintenance of low-level mesocyclones. *Monthly Weather Review*, 122(1), 126–136. [https://doi.org/10.1175/1520-0493\(1994\)122\(0126:TROMWI\)2.0.CO;2](https://doi.org/10.1175/1520-0493(1994)122(0126:TROMWI)2.0.CO;2)
- Brutsaert, W. (1982). *Evaporation into the atmosphere: Theory, history and applications* (Vol. 1). Springer Science & Business Media. <https://doi.org/10.1007/978-94-017-1497-6>
- Chand, K., Sharma, M., & De, A. K. (2022). Effect of inclination angle on heat transport properties in two-dimensional Rayleigh–Bénard convection with smooth and rough boundaries. *Journal of Fluid Mechanics*, 950, A16. <https://doi.org/10.1017/jfm.2022.815>
- Chandrakar, K. K., Cantrell, W., Chang, K., Ciochetto, D., Niedermeier, D., Ovchinnikov, M., et al. (2016). Aerosol indirect effect from turbulence-induced broadening of cloud-droplet size distributions. *Proceedings of the National Academy of Sciences*, 113(50), 14243–14248. <https://doi.org/10.1073/pnas.1612686113>
- Chandrakar, K. K., Cantrell, W., & Shaw, R. A. (2018). Influence of turbulent fluctuations on cloud droplet size dispersion and aerosol indirect effects. *Journal of the Atmospheric Sciences*, 75(9), 3191–3209. <https://doi.org/10.1175/JAS-D-18-0006.1>
- Chandrakar, K. K., Morrison, H., Grabowski, W. W., Bryan, G. H., & Shaw, R. A. (2022). Supersaturation variability from scalar mixing: Evaluation of a new subgrid-scale model using direct numerical simulations of turbulent Rayleigh–Bénard convection. *Journal of the Atmospheric Sciences*, 79(4), 1191–1210. <https://doi.org/10.1175/JAS-D-21-0250.1>
- Chang, K., Bench, J., Brege, M., Cantrell, W., Chandrakar, K., Ciochetto, D., et al. (2016). A laboratory facility to study gas-aerosol-cloud interactions in a turbulent environment: The π chamber. *Bulletin of the American Meteorological Society*, 97(12), 2343–2358. <https://doi.org/10.1175/BAMS-D-15-00203.1>
- Chiu, J. C., Yang, C. K., Van Leeuwen, P. J., Feingold, G., Wood, R., Blanchard, Y., et al. (2021). Observational constraints on warm cloud microphysical processes using machine learning and optimization techniques. *Geophysical Research Letters*, 48(2), e2020GL091236. <https://doi.org/10.1029/2020gl091236>
- Fan, J., Han, B., Varble, A., Morrison, H., North, K., Kollias, P., et al. (2017). Cloud-resolving model intercomparison of an MC3E squall line case: Part I—Convective updrafts. *Journal of Geophysical Research: Atmospheres*, 122(17), 9351–9378. <https://doi.org/10.1002/2017jd026622>
- Garratt, J. R. (1994). *The atmospheric boundary layer*. Cambridge University Press.
- Hill, A. A., Lebo, Z. J., Andrejczuk, M., Arabas, S., Dziekan, P., Field, P., et al. (2023). Toward a numerical benchmark for warm rain processes. *Journal of the Atmospheric Sciences*, 80(5), 1329–1359. <https://doi.org/10.1175/JAS-D-21-0275.1>
- Hsieh, W. C., Jonsson, H., Wang, L.-P., Buzorius, G., Flagan, R. C., Seinfeld, J. H., & Nenes, A. (2009). On the representation of droplet coalescence and autoconversion: Evaluation using ambient cloud droplet size distributions. *Journal of Geophysical Research*, 114(D7), D07201. <https://doi.org/10.1029/2008JD010502>
- Kays, W. M., Crawford, M. E., & Weigand, B. (1980). *Convective heat and mass transfer* (Vol. 4). McGraw-Hill.
- Khain, A., Pokrovsky, A., Pinsky, M., Seifert, A., & Phillips, V. (2004). Simulation of effects of atmospheric aerosols on deep turbulent convective clouds using a spectral microphysics mixed-phase cumulus cloud model. Part I: Model description and possible applications. *Journal of the Atmospheric Sciences*, 61(24), 2963–2982. <https://doi.org/10.1175/JAS-3350.1>

- Khairoutdinov, M. F., & Kogan, Y. (2000). A new cloud physics parameterization in a large-eddy simulation model of marine stratocumulus. *Monthly Weather Review*, 128(1), 229–243. [https://doi.org/10.1175/1520-0493\(2000\)128<0229:ancppi>2.0.co;2](https://doi.org/10.1175/1520-0493(2000)128<0229:ancppi>2.0.co;2)
- Khairoutdinov, M. F., & Randall, D. A. (2003). Cloud resolving modeling of the arm summer 1997 iop: Model formulation, results, uncertainties, and sensitivities. *Journal of the Atmospheric Sciences*, 60(4), 607–625. [https://doi.org/10.1175/1520-0469\(2003\)060\(0607:CRMOTA\)2.0.CO;2](https://doi.org/10.1175/1520-0469(2003)060(0607:CRMOTA)2.0.CO;2)
- Klett, J. D., & Davis, M. H. (1973). Theoretical collision efficiencies of cloud droplets at small Reynolds numbers. *Journal of the Atmospheric Sciences*, 30(1), 107–117. [https://doi.org/10.1175/1520-0469\(1973\)030\(0107:TCEOCD\)2.0.CO;2](https://doi.org/10.1175/1520-0469(1973)030(0107:TCEOCD)2.0.CO;2)
- Kogan, Y. (2013). A cumulus cloud microphysics parameterization for cloud-resolving models. *Journal of the Atmospheric Sciences*, 70(5), 1423–1436. <https://doi.org/10.1175/jas-d-12-0183.1>
- Kolmogorov, A. N. (1941). The local structure of turbulence in incompressible viscous fluid for very large Reynolds numbers. *Comptes rendus de l'Académie des sciences de l'URSS*, 30, 301–305.
- Kostinski, A. B., & Shaw, R. A. (2005). Fluctuations and luck in droplet growth by coalescence. *Bulletin of the American Meteorological Society*, 86(2), 235–244. <https://doi.org/10.1175/bams-86-2-235>
- Kumar, B., Schumacher, J., & Shaw, R. A. (2013). Cloud microphysical effects of turbulent mixing and entrainment. *Theoretical and Computational Fluid Dynamics*, 27(3–4), 361–376. <https://doi.org/10.1007/s00162-012-0272-z>
- Lin, C. L., & Lee, S. C. (1975). Collision efficiency of water drops in the atmosphere. *Journal of the Atmospheric Sciences*, 32(7), 1412–1418. [https://doi.org/10.1175/1520-0469\(1975\)032\(1412:CEOWDI\)2.0.CO;2](https://doi.org/10.1175/1520-0469(1975)032(1412:CEOWDI)2.0.CO;2)
- Long, A. B. (1974). Solutions to droplet collection equation for polynomial kernels. *Journal of the Atmospheric Sciences*, 31(4), 1040–1052. [https://doi.org/10.1175/1520-0469\(1974\)031\(1040:Stdce\)2.0.Co;2](https://doi.org/10.1175/1520-0469(1974)031(1040:Stdce)2.0.Co;2)
- Low, T. B., & List, R. (1982). Collision, coalescence and breakup of raindrops. part ii: Parameterization of fragment size distributions. *Journal of the Atmospheric Sciences*, 39(7), 1607–1619. [https://doi.org/10.1175/1520-0469\(1982\)039\(1607:CCABOR\)2.0.CO;2](https://doi.org/10.1175/1520-0469(1982)039(1607:CCABOR)2.0.CO;2)
- Lu, J., & Shaw, R. A. (2015). Charged particle dynamics in turbulence: Theory and direct numerical simulations. *Physics of Fluids*, 27(6), 065111. <https://doi.org/10.1063/1.4922645>
- Magaritz-Ronen, L., Pinsky, M., & Khain, A. (2016). Drizzle formation in stratocumulus clouds: Effects of turbulent mixing. *Atmospheric Chemistry and Physics*, 16(3), 1849–1862. <https://doi.org/10.5194/acp-16-1849-2016>
- Mallinson, H. M., & Lasher-Trapp, S. G. (2019). An investigation of hydrometeor latent cooling upon convective cold pool formation, sustenance, and properties. *Monthly Weather Review*, 147(9), 3205–3222. <https://doi.org/10.1175/MWR-D-18-0382.1>
- Monin, A., & Obukhov, A. (1954). Basic laws of turbulent mixing in the atmosphere near the ground. *Trudy Geologicheskii Institut, Akademiya Nauk SSSR*, 24, 163–187.
- Morrison, H., Witte, M., Bryan, G. H., Harrington, J. Y., & Lebo, Z. J. (2018). Broadening of modeled cloud droplet spectra using bin microphysics in an Eulerian spatial domain. *Journal of the Atmospheric Sciences*, 75(11), 4005–4030. <https://doi.org/10.1175/JAS-D-18-0055.1>
- Murdzek, S. S., Richardson, Y. P., Markowski, P. M., & Kumjian, M. R. (2022). How the environmental lifting condensation level affects the sensitivity of simulated convective storm cold pools to the microphysics parameterization. *Monthly Weather Review*, 150(10), 2527–2552. <https://doi.org/10.1175/MWR-D-21-0258.1>
- Ng, C. S., Ooi, A., Lohse, D., & Chung, D. (2015). Vertical natural convection: Application of the unifying theory of thermal convection. *Journal of Fluid Mechanics*, 764, 349–361. <https://doi.org/10.1017/jfm.2014.712>
- Niedermeier, D., Chang, K., Cantrell, W., Chandrakar, K. K., Ciochetto, D., & Shaw, R. A. (2018). Observation of a link between energy dissipation rate and oscillation frequency of the large-scale circulation in dry and moist Rayleigh-Bénard turbulence. *Phys. Rev. Fluids*, 3(8), 083501. <https://doi.org/10.1103/PhysRevFluids.3.083501>
- Pinsky, M., Khain, A., & Shapiro, M. (1999). Collisions of small drops in a turbulent flow. Part I: Collision efficiency. Problem formulation and preliminary results. *Journal of the Atmospheric Sciences*, 56(15), 2585–2600. [https://doi.org/10.1175/1520-0469\(1999\)056\(2585:COSDIA\)2.0.CO;2](https://doi.org/10.1175/1520-0469(1999)056(2585:COSDIA)2.0.CO;2)
- Pinsky, M., Khain, A., & Shapiro, M. (2000). Stochastic effects of cloud droplet hydrodynamic interaction in a turbulent flow. *Atmospheric Research*, 53(1), 131–169. [https://doi.org/10.1016/S0169-8095\(99\)00048-4](https://doi.org/10.1016/S0169-8095(99)00048-4)
- Pinsky, M., Khain, A., & Shapiro, M. (2001). Collision efficiency of drops in a wide range of Reynolds numbers: Effects of pressure on spectrum evolution. *Journal of the Atmospheric Sciences*, 58(7), 742–764. [https://doi.org/10.1175/1520-0469\(2001\)058\(0742:CEODIA\)2.0.CO;2](https://doi.org/10.1175/1520-0469(2001)058(0742:CEODIA)2.0.CO;2)
- Pope, S. B. (2000). *Turbulent flows*. Cambridge University Press.
- Prandtl, L. (1933). *Recent results of turbulence research (Technical Memorandums National Advisory Committee for Aeronautics No. 720)*. The National Advisory Committee for Aeronautics.
- Schlamp, R. J., Grover, S. N., Pruppacher, H. R., & Hamielec, A. E. (1976). A numerical investigation of the effect of electric charges and vertical external electric fields on the collision efficiency of cloud drops. *Journal of the Atmospheric Sciences*, 33(9), 1747–1755. [https://doi.org/10.1175/1520-0469\(1976\)033\(1747:ANIOTE\)2.0.CO;2](https://doi.org/10.1175/1520-0469(1976)033(1747:ANIOTE)2.0.CO;2)
- Schmeissner, T., Shaw, R. A., Ditas, J., Stratmann, F., Wendisch, M., & Siebert, H. (2015). Turbulent mixing in shallow trade wind cumuli: Dependence on cloud life cycle. *Journal of the Atmospheric Sciences*, 72(4), 1447–1465. <https://doi.org/10.1175/JAS-D-14-0230.1>
- Schumann, U., & Moeng, C.-H. (1991). Plume fluxes in clear and cloudy convective boundary layers. *Journal of the Atmospheric Sciences*, 48(15), 1746–1757. [https://doi.org/10.1175/1520-0469\(1991\)048\(1746:PFICAC\)2.0.CO;2](https://doi.org/10.1175/1520-0469(1991)048(1746:PFICAC)2.0.CO;2)
- Seifert, A., Khain, A., Blahak, U., & Beheng, K. D. (2005). Possible effects of collisional breakup on mixed-phase deep convection simulated by a spectral (bin) cloud model. *Journal of the Atmospheric Sciences*, 62(6), 1917–1931. <https://doi.org/10.1175/JAS3432.1>
- Shaw, R. A., Cantrell, W., Chen, S., Chuang, P., Donahue, N., Feingold, G., et al. (2020). Cloud-aerosol-turbulence interactions: Science priorities and concepts for a large-scale laboratory facility. *Bulletin of the American Meteorological Society*, 101(7), E1026–E1035. <https://doi.org/10.1175/BAMS-D-20-0009.1>
- Shishkina, O. (2016). Momentum and heat transport scalings in laminar vertical convection. *Physical Review E*, 93(5), 051102. <https://doi.org/10.1103/physreve.93.051102>
- Smolarkiewicz, P. K., & Grabowski, W. W. (1990). The multidimensional positive definite advection transport algorithm: Nonoscillatory option. *Journal of Computational Physics*, 86(2), 355–375. [https://doi.org/10.1016/0021-9991\(90\)90105-A](https://doi.org/10.1016/0021-9991(90)90105-A)
- Stensrud, D. J. (2007). Microphysics parameterizations. In *Parameterization schemes: Keys to understanding numerical weather prediction models* (pp. 260–305). Cambridge University Press. <https://doi.org/10.1017/CBO9780511812590.008>
- Szopa, S., Naik, V., Adhikary, B., Artaxo, P., Bernsten, T., Collins, W., et al. (2021). Short-lived climate forcers. In V. Masson-Delmotte, P. Zhai, A. Pirani, S. L. Connors, C. Péan, S. Berger, et al. (Eds.), *Climate change 2021: The physical science basis. Contribution of working group I to the sixth assessment report of the intergovernmental panel on climate change* (pp. 817–922). Cambridge University Press. <https://doi.org/10.1017/9781009157896.008>

- Thomas, S., Ovchinnikov, M., Yang, F., van der Voort, D., Cantrell, W., Krueger, S. K., & Shaw, R. A. (2019). Scaling of an atmospheric model to simulate turbulence and cloud microphysics in the pi chamber. *Journal of Advances in Modeling Earth Systems*, *11*(7), 1981–1994. <https://doi.org/10.1029/2019MS001670>
- Thomas, S., Prabhakaran, P., Yang, F., Cantrell, W. H., & Shaw, R. A. (2022). Dimensionless parameters for cloudy Rayleigh–bénard convection: Supersaturation, damköhler, and nusselt numbers. *Physical Review Fluids*, *7*(1), 010503. <https://doi.org/10.1103/physrevfluids.7.010503>
- Thomas, S., Yang, F., Ovchinnikov, M., Cantrell, W. H., & Shaw, R. A. (2023). Scaling of turbulence and microphysics in a convection–cloud chamber of varying height. *Journal of Advances in Modeling Earth Systems*, *15*(2), e2022MS003304. <https://doi.org/10.1029/2022MS003304>
- Toppaladoddi, S., Succi, S., & Wettlaufer, J. S. (2015). Tailoring boundary geometry to optimize heat transport in turbulent convection. *Europhysics Letters*, *111*(4), 44005. <https://doi.org/10.1209/0295-5075/111/44005>
- Tummers, M. J., & Steunebrink, M. (2019). Effect of surface roughness on heat transfer in Rayleigh–Bénard convection. *International Journal of Heat and Mass Transfer*, *139*, 1056–1064. <https://doi.org/10.1016/j.ijheatmasstransfer.2019.05.066>
- Wang, A., Pan, Y., & Markowski, P. M. (2021). The influence of weno schemes on large-eddy simulations of a neutral atmospheric boundary layer. *Journal of the Atmospheric Sciences*, *78*, 3613–3628. <https://doi.org/10.1175/JAS-D-21-0033.1>
- Wang, A., Yang, X. I. A., & Ovchinnikov, M. (2023). An investigation of LES wall modeling for Rayleigh–Bénard convection via interpretable and physics-aware feedforward neural networks with DNS. *Journal of the Atmospheric Sciences*. in press. <https://doi.org/10.1175/jas-d-23-0094.1>
- Wang, Q., Liu, H.-R., Verzicco, R., Shishkina, O., & Lohse, D. (2021). Regime transitions in thermally driven high-Rayleigh number vertical convection. *Journal of Fluid Mechanics*, *917*, A6. <https://doi.org/10.1017/jfm.2021.262>
- Wood, R. (2006). Rate of loss of cloud droplets by coalescence in warm clouds. *Journal of Geophysical Research*, *111*(D21), D21205. <https://doi.org/10.1029/2006jd007553>
- Yang, F., Hoffmann, F., Shaw, R. A., Ovchinnikov, M., & Vogelmann, A. M. (2023). An intercomparison of large-eddy simulations of a convection cloud chamber using haze-capable bin and Lagrangian cloud microphysics schemes. *Journal of Advances in Modeling Earth Systems*, *15*(5), e2022MS003270. <https://doi.org/10.1029/2022ms003270>
- Yang, F., Ovchinnikov, M., Thomas, S., Khain, A., McGraw, R., Shaw, R. A., & Vogelmann, A. M. (2022). Large-eddy simulations of a convection cloud chamber: Sensitivity to bin microphysics and advection. *Journal of Advances in Modeling Earth Systems*, *14*(5), e2021MS002895. <https://doi.org/10.1029/2021ms002895>
- Zhu, X., Stevens, R. J. A. M., Shishkina, O., Verzicco, R., & Lohse, D. (2019). $Nu \sim Ra^{1/2}$ scaling enabled by multiscale wall roughness in Rayleigh–Bénard turbulence. *Journal of Fluid Mechanics*, *869*, R4. <https://doi.org/10.1017/jfm.2019.228>